Fig. 21.50 Chart for determining optimal film thickness. (From Ref. 28.) (a) Grooved member rotating. (b) Smooth member rotating.

6. Calculate

$$\frac{R_1}{h_r} = \left\{ \frac{\Lambda_c p_a}{3\eta(\omega_h - \omega_o)[1 - (R_2/R_1)^2]} \right\}^{1/2}$$

If $R_1/h_r > 10,000$ (or whatever preassigned radius-to-clearance ratio), a larger bearing or higher speed is required. Return to step 2. If these changes cannot be made, an externally pressurized bearing must be used.

7. Having established what α_r and Λ_c should be, obtain values of $\overline{K}_\infty$, $\overline{Q}$, and $\overline{T}$ from Figs. 21.62, 21.63, and 21.64, respectively. From Eqs. (21.29), (21.30), and (21.31) calculate K_p, Q, and T_r.

8. From Fig. 21.65 obtain groove geometry (b, β_a, and H_a) and from Fig. 21.66 obtain R_g.

21.3 ELASTOHYDRODYNAMIC LUBRICATION

Downson[31] defines elastohydrodynamic lubrication (EHL) as "the study of situations in which elastic deformation of the surrounding solids plays a significant role in the hydrodynamic lubrication process." Elastohydrodynamic lubrication implies complete fluid-film lubrication and no asperity interaction of the surfaces. There are two distinct forms of elastohydrodynamic lubrication.

1. *Hard EHL.* Hard EHL relates to materials of high elastic modulus, such as metals. In this form of lubrication not only are the elastic deformation effects important, but the pressure–viscosity
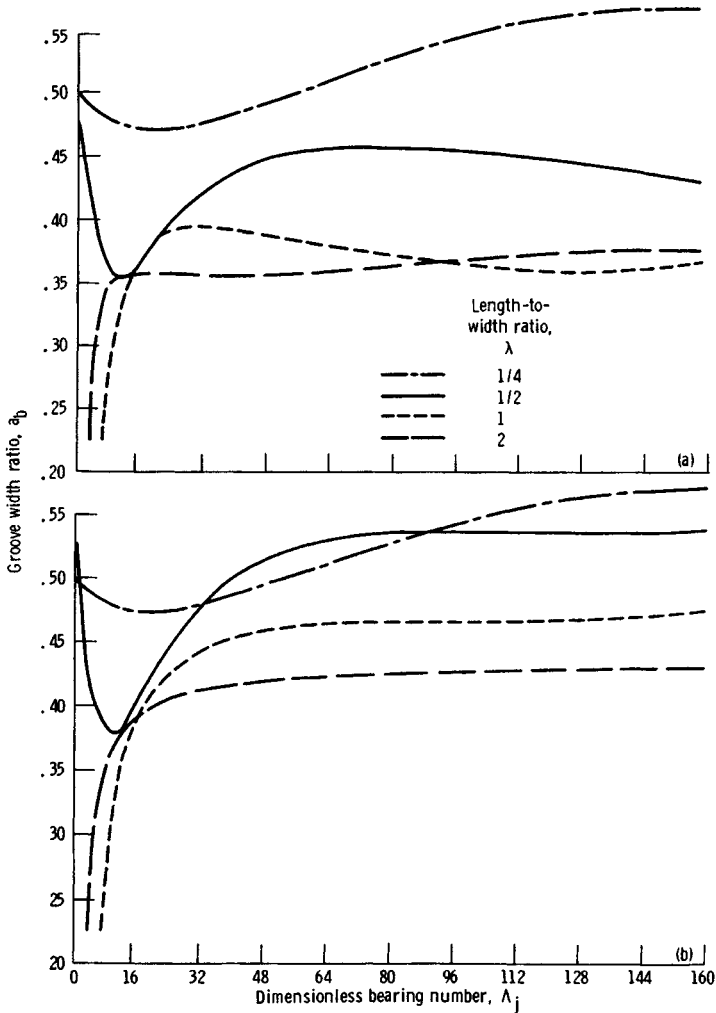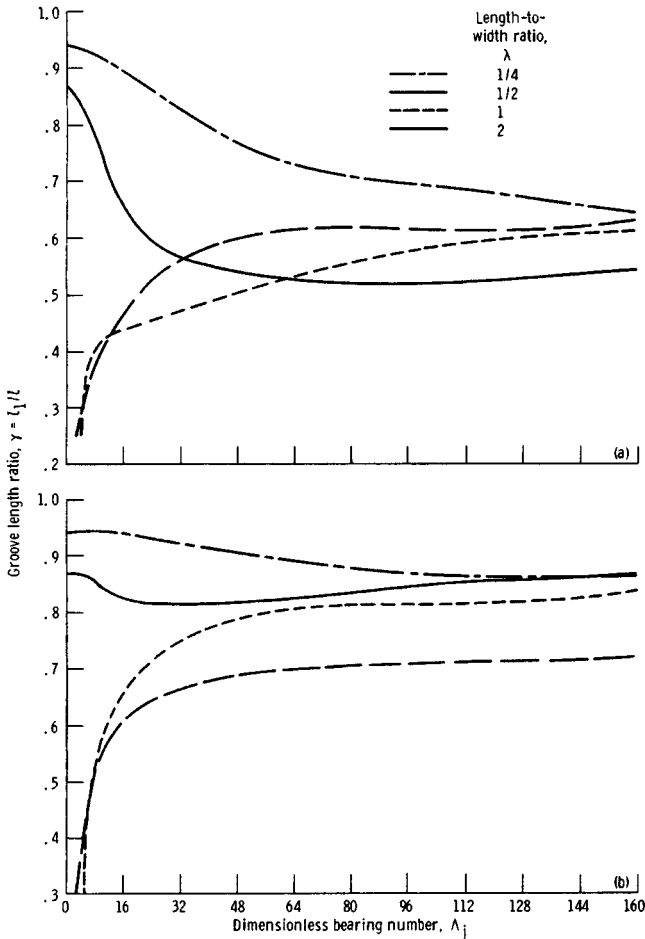
Fig. 21.51   Chart for determining optimal groove width ratio. (From Ref. 28.) (a) Grooved member rotating. (b) Smooth member rotating.

effects are equally as important. Engineering applications in which this form of lubrication is dominant include gears and rolling-element bearings.

2. *Soft EHL.*   Soft EHL relates to materials of low elastic modulus, such as rubber. For these materials that elastic distortions are large, even with light loads. Another feature is the negligible pressure–viscosity effect on the lubricating film. Engineering applications in which soft EHL is important include seals, human joints, tires, and a number of lubricated elastomeric material machine elements.

The recognition and understanding of elastohydrodynamic lubrication presents one of the major developments in the field of tribology in this century. The revelation of a previously unsuspected regime of lubrication is clearly an event of importance in tribology. Elastohydrodynamic lubrication not only explained the remarkable physical action responsible for the effective lubrication of many machine elements, but it also brought order to the understanding of the complete spectrum of lubrication regimes, ranging from boundary to hydrodynamic.

A way of coming to an understanding of elastohydrodynamic lubrication is to compare it to hydrodynamic lubrication. The major developments that have led to our present understanding of hydrodynamic lubrication[1,3] predate the major developments of elastohydrodynamic lubrication[32,33]

Fig. 21.52   Chart for determining optimal groove length ratio. (From Ref. 28.) (a) Grooved member rotating. (b) Smooth member rotating.

by 65 years. Both hydrodynamic and elastohydrodynamic lubrication are considered as fluid-film lubrication in that the lubricant film is sufficiently thick to prevent the opposing solids from coming into contact. Fluid-film lubrication is often referred to as the ideal form of lubrication since it provides low friction and high resistance to wear.

This section highlights some of the important aspects of elastohydrodynamic lubrication while illustrating its use in a number of applications. It is not intended to be exhaustive but to point out the significant features of this important regime of lubrication. For more details the reader is referred to Hamrock and Dowson.[10]

21.3.1   Contact Stresses and Deformations

As was pointed out in Section 21.1.1, elastohydrodynamic lubrication is the mode of lubrication normally found in nonconformal contacts such as rolling-element bearings. A load–deflection relationship for nonconformal contacts is developed in this section. The deformation within the contact is calculated from, among other things, the ellipticity parameter and the elliptic integrals of the first and second kinds. Simplified expressions that allow quick calculations of the stresses and deformations to be made easily from a knowledge of the applied load, the material properties, and the geometry of the contacting elements are presented in this section.

Elliptical Contacts

The undeformed geometry of contacting solids in a nonconformal contact can be represented by two ellipsoids. The two solids with different radii of curvature in a pair of principal planes (x and y)
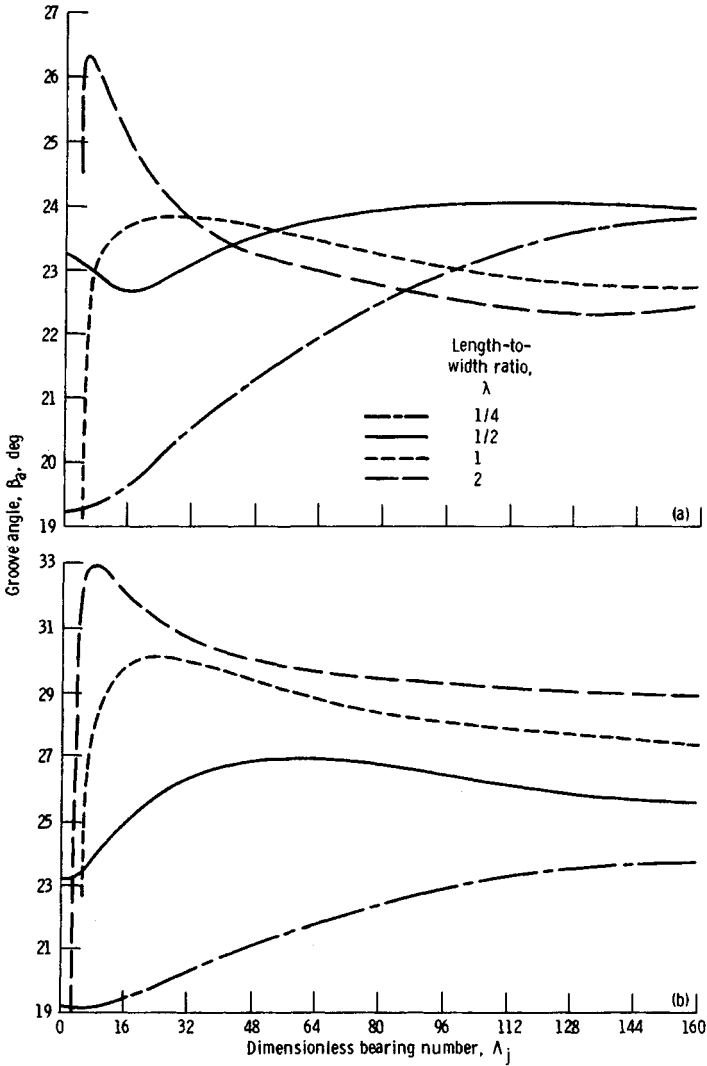
Fig. 21.53 Chart for determining optimal groove angle. (From Ref. 28.) (a) Grooved member rotating. (b) Smooth member rotating.

passing through the contact between the solids make contact at a single point under the condition of zero applied load. Such a condition is called point contact and is shown in Fig. 21.67, where the radii of curvature are denoted by r's. It is assumed that convex surfaces, as shown in Fig. 21.67, exhibit positive curvature and concave surfaces exhibit negative curvature. Therefore if the center of curvature lies within the solids, the radius of curvature is positive; if the center of curvature lies outside the solids, the radius of curvature is negative. It is important to note that if coordinates x and y are chosen such that

$$\frac{1}{r_{ax}} + \frac{1}{r_{bx}} > \frac{1}{r_{ay}} + \frac{1}{r_{by}} \tag{21.33}$$

coordinate x then determines the direction of the semiminor axis of the contact area when a load is applied and y determines the direction of the semimajor axis. The direction of motion is always considered to be along the x axis.
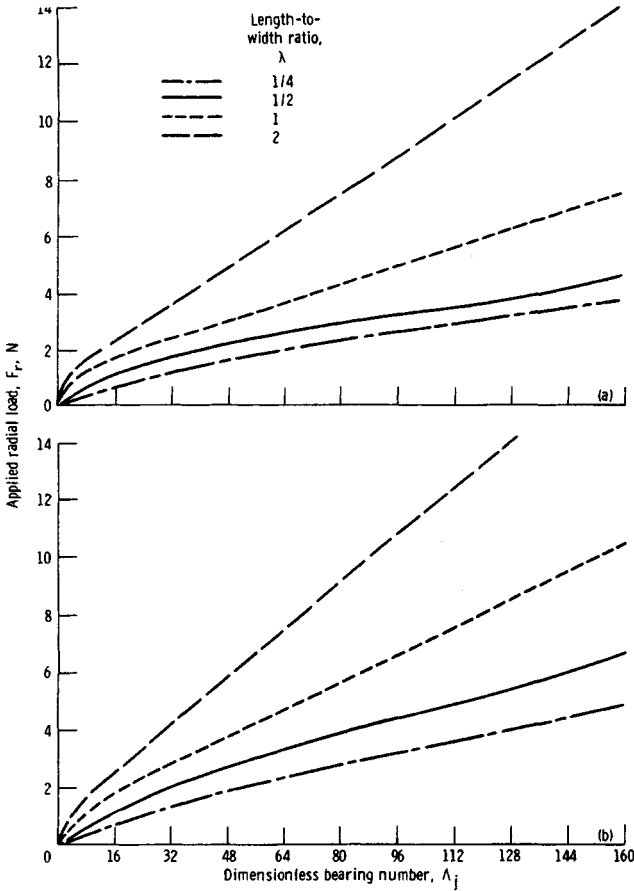
Fig. 21.54   Chart for determining maximum radial load capacity. (From Ref. 28.) (a) Grooved member rotating. (b) Smooth member rotating.

The curvature sum and difference, which are quantities of some importance in the analysis of contact stresses and deformations, are

$$\frac{1}{R} = \frac{1}{R_x} + \frac{1}{R_y} \tag{21.34}$$

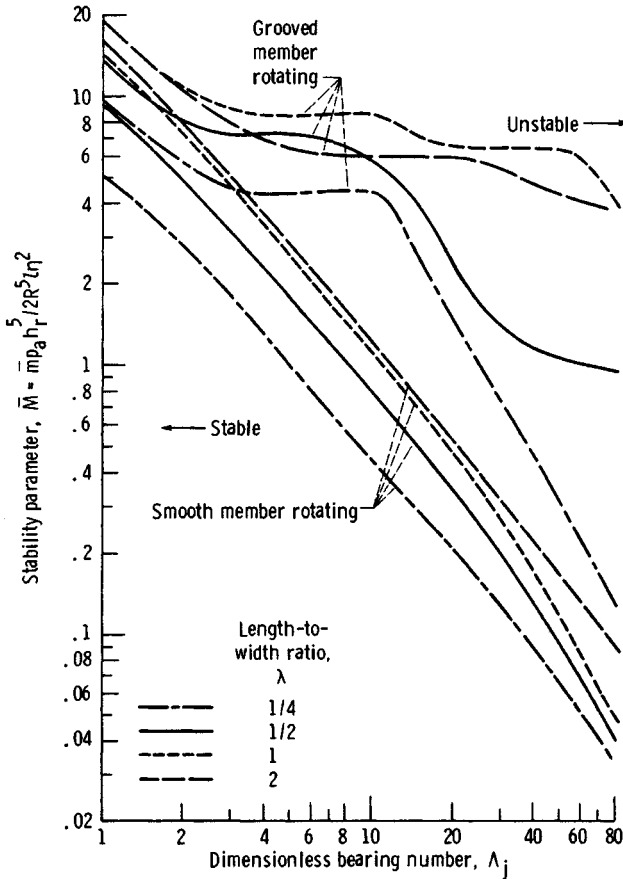$$\Gamma = R\left(\frac{1}{R_x} - \frac{1}{R_y}\right) \tag{21.35}$$

where

$$\frac{1}{R_x} = \frac{1}{r_{ax}} + \frac{1}{r_{bx}} \tag{21.36}$$

$$\frac{1}{R_y} = \frac{1}{r_{ay}} + \frac{1}{r_{by}} \tag{21.37}$$

$$\alpha = \frac{R_y}{R_x} \tag{21.38}$$

Equations (21.36) and (21.37) effectively redefine the problem of two ellipsoidal solids approaching one another in terms of an equivalent ellipsoidal solid of radii R_x and R_y approaching a plane.

Fig. 21.55 Chart for determining maximum stability of herringbone-groove bearings. (From Ref. 29.)

The ellipticity parameter k is defined as the elliptical-contact diameter in the y direction (transverse direction) divided by the elliptical-contact diameter in the x direction (direction of motion) or $k = D_y/D_x$. If Eq. (21.33) is satisfied and $\alpha \geq 1$, the contact ellipse will be oriented so that its major diameter will be transverse to the direction of motion, and, consequently, $k \geq 1$. Otherwise, the major diameter would lie along the direction of motion with both $\alpha \leq 1$ and $k \leq 1$. Figure 21.68 shows the ellipticity parameter and the elliptic integrals of the first and second kinds for a range of curvature ratios ($\alpha = R_y/R_x$) usually encountered in concentrated contacts.

Simplified Solutions for $\alpha > 1$. The classical Hertzian solution requires the calculation of the ellipticity parameter k and the complete elliptic integrals of the first and second kinds $\mathcal{F}$ and $\mathcal{E}$. This entails finding a solution to a transcendental equation relating k, $\mathcal{F}$, and $\mathcal{E}$ to the geometry of the contacting solids. Possible approaches include an iterative numerical procedure, as described, for example, by Hamrock and Anderson,[35] or the use of charts, as shown by Jones.[36] Hamrock and Brewe[34] provide a shortcut to the classical Hertzian solution for the local stress and deformation of two elastic bodies in contact. The shortcut is accomplished by using simplified forms of the ellipticity parameter and the complete elliptic integrals, expressing them as functions of the geometry. The results of Hamrock and Brewe's work[34] are summarized here.

A power fit using linear regression by the method of least squares resulted in the following expression for the ellipticity parameter:

$$k = \alpha^{2/\pi}, \quad \text{for} \quad \alpha \geq 1 \tag{21.39}$$

The asymptotic behavior of $\mathcal{E}$ and $\mathcal{F}$ ($\alpha \to 1$ implies $\mathcal{E} \to \mathcal{F} \to \pi/2$, and $\alpha \to \infty$ implies $\mathcal{F} \to \infty$ and
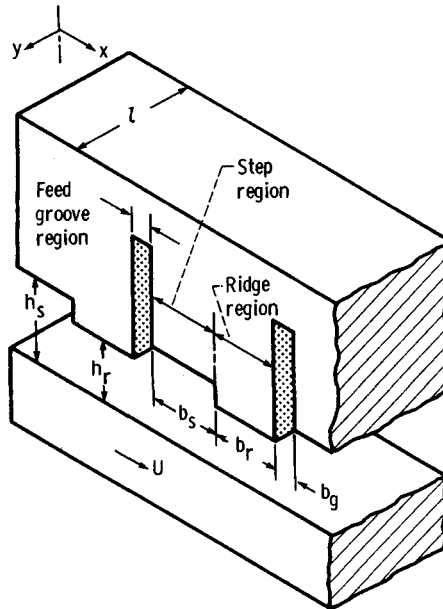
Fig. 21.56 Configuration of rectangular step thrust bearing. (From Ref. 30.)

$\mathscr{E} \to 1$) was suggestive of the type of functional dependence that $\mathscr{E}$ and $\mathscr{F}$ might follow. As a result, an inverse and a logarithmic fit were tried for $\mathscr{E}$ and $\mathscr{F}$, respectively. The following expressions provided excellent curve fits:

$$\mathscr{E} = 1 + \frac{q}{\alpha} \qquad \text{for} \quad \alpha \geq 1 \tag{21.40}$$

$$\mathscr{F} = \frac{\pi}{2} + q \ln \alpha \qquad \text{for} \quad \alpha \geq 1 \tag{21.41}$$

where

$$q = \frac{\pi}{2} - 1 \tag{21.42}$$

When the ellipticity parameter k [Eq. (21.39)], the elliptic integrals of the first and second kinds [Eqs. (21.40) and (21.41)], the normal applied load F, Poisson's ratio ν, and the modulus of elasticity E of the contacting solids are known, we can write the major and minor axes of the contact ellipse and the maximum deformation at the center of the contact, from the analysis of Hertz,[37] as

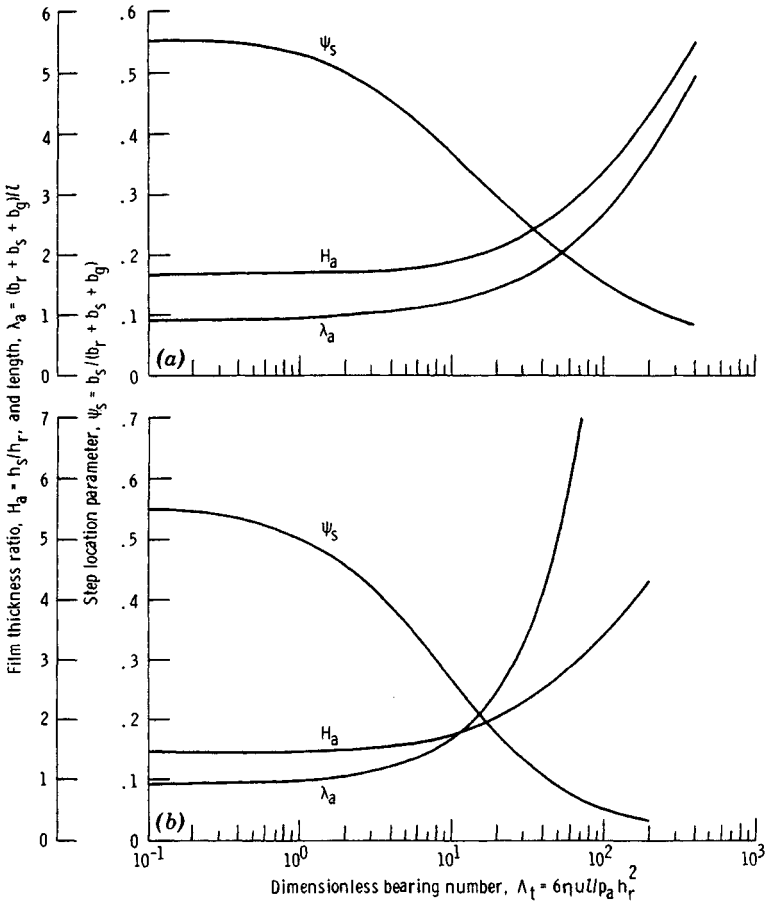$$D_y = 2 \left(\frac{6k^2 \mathscr{E} F R}{\pi E'} \right)^{1/3} \tag{21.43}$$

$$D_x = 2 \left(\frac{6 \mathscr{E} F R}{\pi k E'} \right)^{1/3} \tag{21.44}$$

$$\delta = F \left[\left(\frac{9}{2 \mathscr{E} R} \right) \left(\frac{F}{\pi k E'} \right)^2 \right]^{1/3} \tag{21.45}$$

where [as in Eq. (21.12)]

$$E' = 2 \left(\frac{1 - \nu_a^2}{E_a} + \frac{1 - \nu_b^2}{E_b} \right)^{-1} \tag{21.46}$$

In these equations D_y and D_x are proportional to $F^{1/3}$ and δ is proportional to $F^{2/3}$.

Fig. 21.57 Chart for determining optimal step parameters. (From Ref. 30.) (a) Maximum dimensionless load. (b) Maximum dimensionless stiffness.

The maximum Hertzian stress at the center of the contact can also be determined by using Eqs. (21.42) and (21.44)

$$\sigma_{max} = \frac{6F}{\pi D_x D_y} \tag{21.47}$$

Simplified Solutions for $\alpha \leq 1$. Table 21.7 gives the simplified equations for $\alpha < 1$ as well as for $\alpha \geq 1$. Recall that $\alpha \geq 1$ implies $k \geq 1$ and Eq. (21.33) is satisfied, and $\alpha < 1$ implies $k < 1$ and Eq. (21.33) is not satisfied. It is important to make the proper evaluation of α, since it has a great significance in the outcome of the simplified equations.

Figure 21.69 shows three diverse situations in which the simplified equations can be usefully applied. The locomotive wheel on a rail (Fig. 21.69a) illustrates an example in which the ellipticity parameter k and the radius ratio α are less than 1. The ball rolling against a flat plate (Fig. 21.69b) provides pure circular contact (i.e., $\alpha = k = 1.0$). Figure 21.69c shows how the contact ellipse is formed in the ball–outer-race contact of a ball bearing. Here the semimajor axis is normal to the direction of rolling and, consequently, α and k are greater than 1. Table 21.8 shows how the degree of conformity affects the contact parameters for the various cases illustrated in Fig. 21.69.

Rectangular Contacts

For this situation the contact ellipse discussed in the preceding section is of infinite length in the transverse direction ($D_y \rightarrow \infty$). This type of contact is exemplified by a cylinder loaded against a
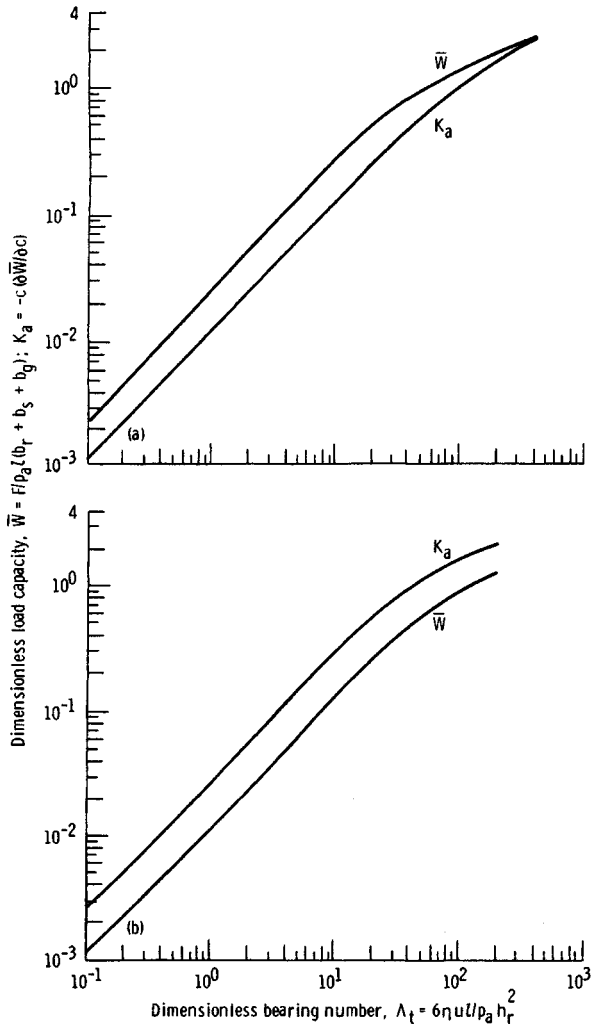
Fig. 21.58 Chart for determining dimensionless load capacity and stiffness. (From Ref. 30.) (a) Maximum dimensionless load capacity. (b) Maximum stiffness.

plate, a groove, or another parallel cylinder or by a roller loaded against an inner or outer ring. In these situations the contact semiwidth is given by

$$b = R_x \left(\frac{8W}{\pi} \right)^{1/2} \tag{21.48}$$

where

$$W = \frac{F'}{E' R_x} \tag{21.49}$$

and F' is the load per unit length along the contact.

The maximum deformation due to the approach of centers of two cylinders can be written as[12]
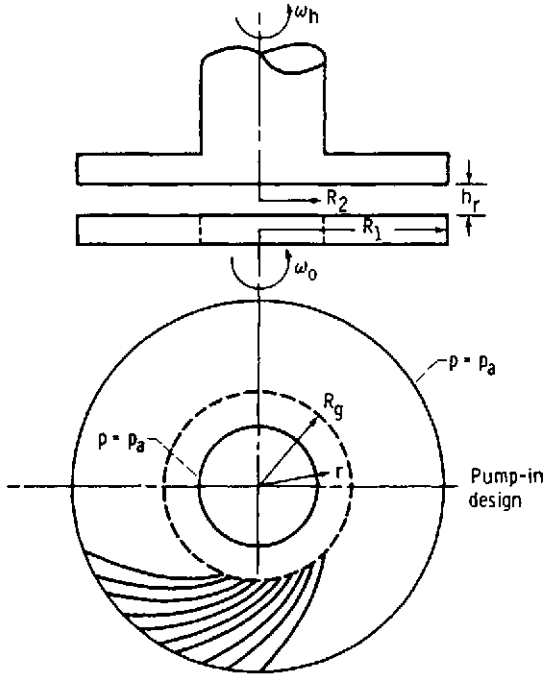
Fig. 21.59 Configuration of spiral-groove thrust bearing. (From Ref. 20.)
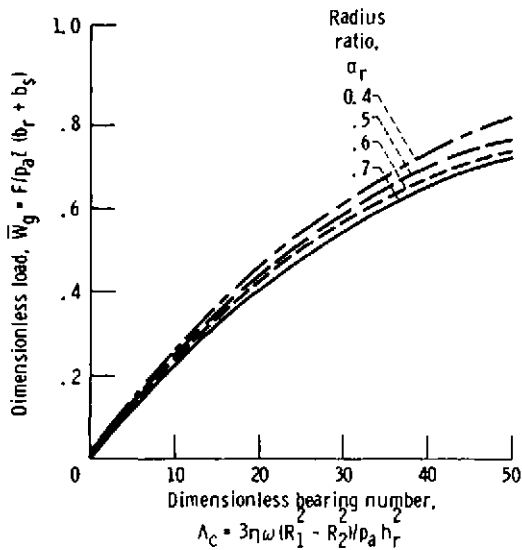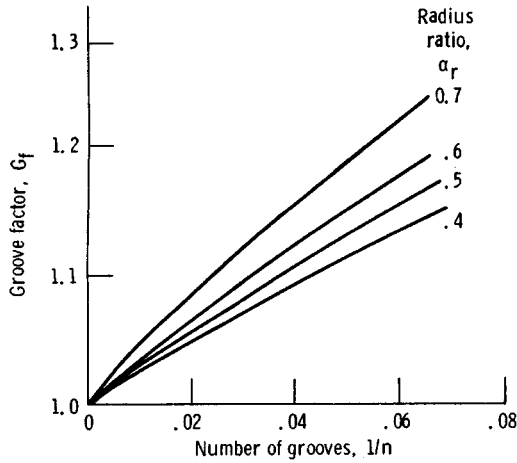

Fig. 21.60 Chart for determining load for spiral-groove thrust bearings. (From Ref. 20.)

Fig. 21.61 Chart for determining groove factor for spiral-groove thrust bearings. (From Ref. 20.)

$$\delta = \frac{2WR_x}{\pi} \left[\frac{2}{3} + \ln\left(\frac{2r_{ax}}{b}\right) + \ln\left(\frac{2r_{bx}}{b}\right) \right]$$ (21.50)

The maximum Hertzian stress in a rectangular contact can be written as

$$\sigma_{\max} = E' \left(\frac{W}{2\pi}\right)^{1/2}$$ (21.51)

21.3.2 Dimensionless Grouping
The variables appearing in elastohydrodynamic lubrication theory are

E' = effective elastic modulus, N/m^2
F = normal applied load, N
h = film thickness, m
R_x = effective radius in x (motion) direction, m
R_y = effective radius in y (transverse) direction, m
u = mean surface velocity in x direction, m/sec
ξ = pressure–viscosity coefficient of fluid, m^2/N
η_0 = atmospheric viscosity, N sec/m^2;

From these variables the following five dimensionless groupings can be established.
Dimensionless film thickness

$$H = \frac{h}{R_x}$$ (21.52)

Ellipticity parameter

$$k = \frac{D_y}{D_x} = \left(\frac{R_y}{R_x}\right)^{2/\pi}$$ (21.53)

Dimensionless load parameter

$$W = \frac{F}{E'R_x^2}$$ (21.54)

Dimensionless speed parameter
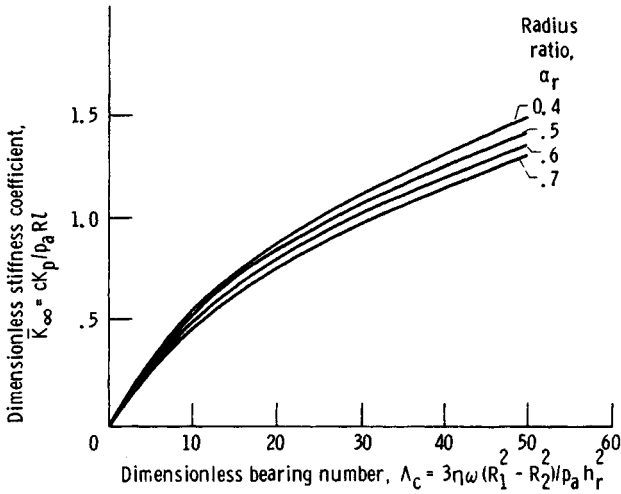
Fig. 21.62 Chart for determining stiffness for spiral-groove thrust bearings. (From Ref. 20.)

$$U = \frac{\eta_0 u}{E' R_x} \tag{21.55}$$

Dimensionless materials parameter

$$G = \xi E' \tag{21.56}$$

The dimensionless minimum film thickness can now be written as a function of the other parameters involved:

$$H = f(k, U, W, G)$$

The most important practical aspect of elastohydrodynamic lubrication theory becomes the deter-

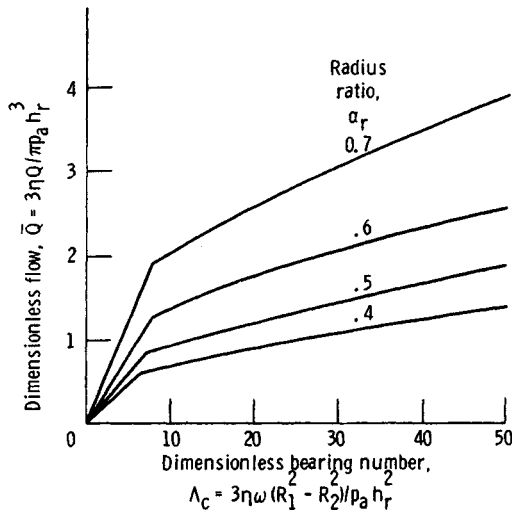**Fig. 21.63** Chart for determining flow for spiral-groove thrust bearings. (From Ref. 20.)
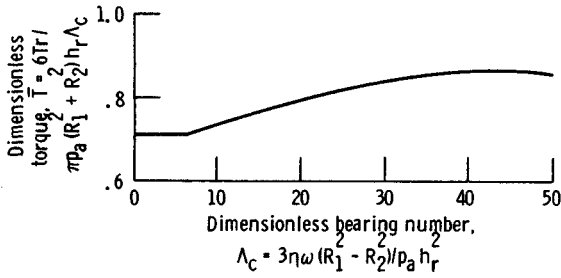
Fig. 21.64 Chart for determining torque for spiral-groove thrust bearings. (Curve is for all radius ratios. From Ref. 20.)

mination of this function f for the case of the minimum film thickness within a conjunction. Maintaining a fluid-film thickness of adequate magnitude is clearly vital to the efficient operation of machine elements.

21.3.3 Hard-EHL Results

By using the numerical procedures outlined in Hamrock and Dowson,[38] the influence of the ellipticity parameter and the dimensionless speed, load, and materials parameters on minimum film thickness was investigated by Hamrock and Dowson.[39] The ellipticity parameter k was varied from 1 (a ball-on-plate configuration) to 8 (a configuration approaching a rectangular contact). The dimensionless speed parameter U was varied over a range of nearly two orders of magnitude, and the dimensionless load parameter W over a range of one order of magnitude. Situations equivalent to using materials of bronze, steel, and silicon nitride and lubricants of paraffinic and naphthenic oils were considered in the investigation of the role of the dimensionless materials parameter G. Thirty-four cases were used in generating the minimum-film-thickness formula for hard EHL given here:

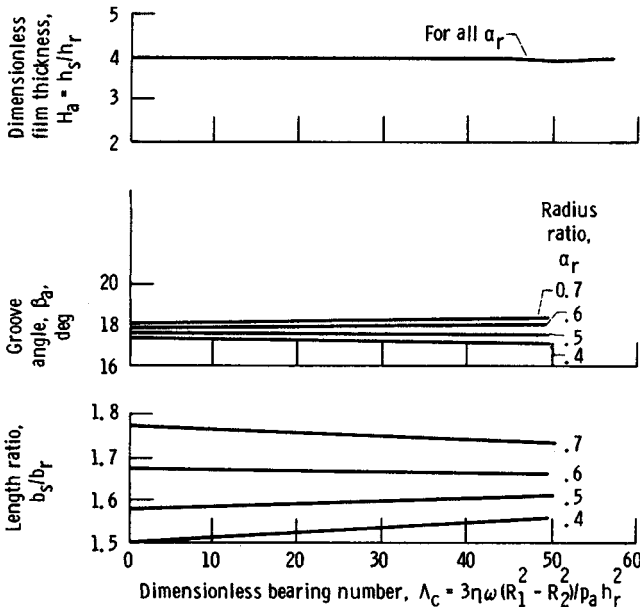$$H_{\min} = 3.63 \, U^{0.68}G^{0.49}W^{-0.073}(1 - e^{-0.68k}) \tag{21.57}$$

Fig. 21.65 Chart for determining optimal groove geometry for spiral-groove thrust bearings. (from Ref. 20.)
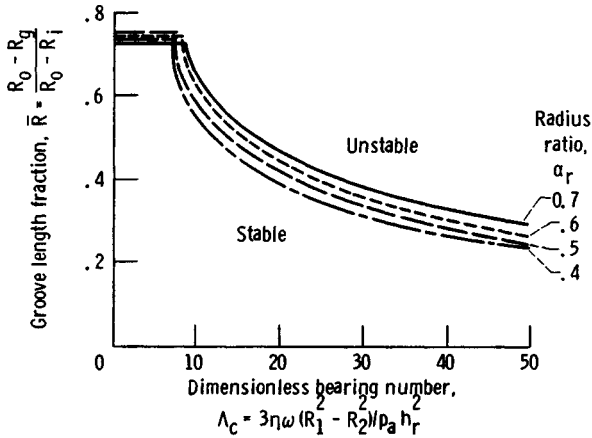
Fig. 21.66 Chart for determining groove length fraction for spiral-groove thrust bearings. (From Ref. 20.)

In this equation the dominant exponent occurs on the speed parameters, while the exponent on the load parameter is very small and negative. The materials parameter also carries a significant exponent, although the range of this variable in engineering situations is limited.

In addition to the minimum-film-thickness formula, contour plots of pressure and film thickness throughout the entire conjunction can be obtained from the numerical results. A representative contour plot of dimensionless pressure is shown in Fig. 21.70 for $k = 1.25$, $U = 0.168 \times 10^{-11}$, and $G = 4522$. In this figure and in Fig. 21.71, the $+$ symbol indicates the center of the Hertzian contact zone. The dimensionless representation of the X and Y coordinates causes the actual Hertzian contact ellipse to be a circle regardless of the value of the ellipticity parameter. The Hertzian contact circle is shown by asterisks. On this figure is a key showing the contour labels and each corresponding value of dimensionless pressure. The inlet region is to the left and the exit region is to the right. The pressure gradient at the exit end of the conjunction is much larger than that in the inlet region. In Fig. 21.70 a pressure spike is visible at the exit of the contact.

Fig. 21.67 Geometry of contacting elastic solids. (From Ref. 10.)

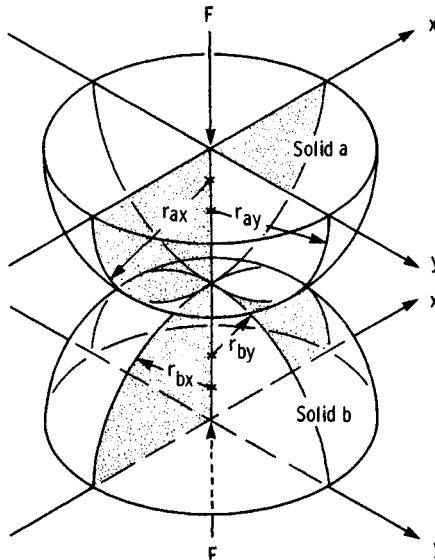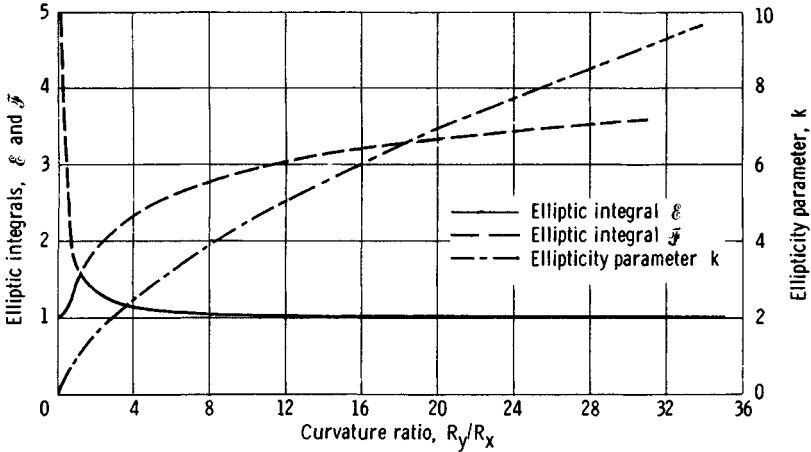**Fig. 21.68**   Chart for determining ellipticity parameter and elliptic integrals of first and second kinds. (From Ref. 34.)

Contour plots of the film thickness are shown in Fig. 21.71 for the same case as Fig. 21.70. In this figure two minimum regions occur in well-defined lobes that follow, and are close to, the edge of the Hertzian contact circle. These results contain all of the essential features of available experimental observations based on optical interferometry.[40]

Table 21.7   Simplified Equations (From Ref. 6)

$a \geq 1$	$a < 1$
$\bar{k} = \alpha^{2/\pi}$	$\bar{k} = \alpha^{2/\pi}$
$\bar{\mathfrak{F}} = \dfrac{\pi}{2} + q \ln \alpha$	$\bar{\mathfrak{F}} = \dfrac{\pi}{2} + q \ln \alpha$
where $q = \dfrac{\pi}{2} - 1$	where $q = \dfrac{\pi}{2} - 1$
$\bar{\mathcal{E}} = 1 + \dfrac{q}{\alpha}$	$\bar{\mathcal{E}} = 1 + q\alpha$
$D_y = 2\left(\dfrac{6k^2\,\mathcal{E}FR}{\pi E'}\right)^{1/3}$	$D_y = 2\left(\dfrac{6k\,\mathcal{E}FR}{\pi E'}\right)^{1/3}$
where $R^{-1} = R_x^{-1} + R_y^{-1}$	where $R^{-1} = R_x^{-1} + R_y^{-1}$
$D_x = 2\left(\dfrac{6\,\mathcal{E}FR}{\pi k E'}\right)^{1/3}$	$D_x = 2\left(\dfrac{6\,\mathcal{E}FR}{\pi E'k^2}\right)^{1/3}$
$\delta = \mathfrak{F}\left[\left(\dfrac{4.5}{\mathcal{E}R}\right)\left(\dfrac{F}{\pi k E'}\right)^2\right]^{1/3}$	$\delta = \mathfrak{F}\left[\left(\dfrac{4.5}{\mathcal{E}R}\right)\left(\dfrac{F}{\pi E'}\right)^2\right]^{1/3}$

(a)

(b)

(c)

Fig. 21.69 Three degrees of conformity. (From Ref. 34.) (a) Wheel on rail. (b) Ball on plane. (c) Ball–outer-race contact.

Table 21.8   Practical Applications for Differing Conformities[a] (From Ref. 34)

Contact Parameters	Wheel on Rail	Ball on Plane	Ball-Outer-Race Contact
F	1.00×10^5 N	222.4111 N	222.4111 N
r_{ax}	50.1900 cm	0.6350 cm	0.6350 cm
r_{ay}	∞	0.6350 cm	0.6350 cm
r_{bx}	∞	∞	-3.8900 cm
r_{by}	30.0000 cm	∞	-0.6600 cm
u	0.5977	1.0000	22.0905
k	0.7206	1.0000	7.1738
$\mathcal{E}$	1.3412	1.5708	1.0258
$\mathcal{F}$	1.8645	1.5708	3.3375
D_y	1.0807 cm	0.0426 cm	0.1810 cm
D_x	1.4997 cm	0.0426 cm	0.0252 cm
δ	0.0108 cm	7.13×10^{-4} cm	3.57×10^{-4} cm
σ_{max}	1.1784×10^5 N/cm^2	2.34×10^5 N/cm^2	9.30×10^4 N/cm^2

[a]$E' = 2.197 \times 10^7$ N/cm^2.

21.3.4   Soft-EHL Results

In a similar manner, Hamrock and Dowson[41] investigated the behavior of soft-EHL contacts. The ellipticity parameter was varied from 1 (a circular configuration) to 12 (a configuration approaching a rectangular contact), while U and W were varied by one order of magnitude and there were two different dimensionless materials parameters. Seventeen cases were considered in obtaining the dimensionless minimum-film-thickness equation for soft EHL:

$$H_{min} = 7.43U^{0.65}W^{-0.21}(1 - 0.85e^{-0.31k}) \qquad (21.58)$$

The powers of U in Eqs. (21.57) and (21.58) are quite similar, but the power of W is much more
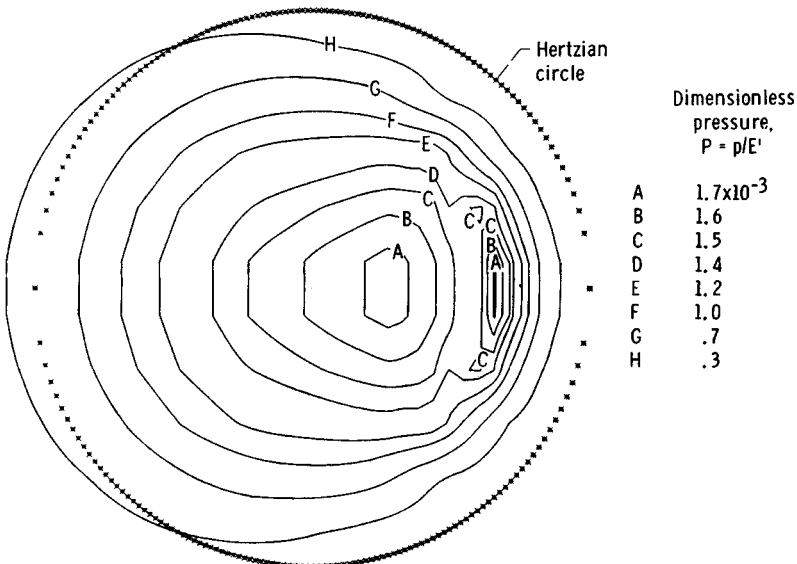
Fig. 21.70   Contour plot of dimensionless pressure. $k = 1.25$; $U = 0.168 \times 10^{-11}$; $W = 0.111 \times 10^{-6}$; $G = 4522$. (From Ref. 39.)
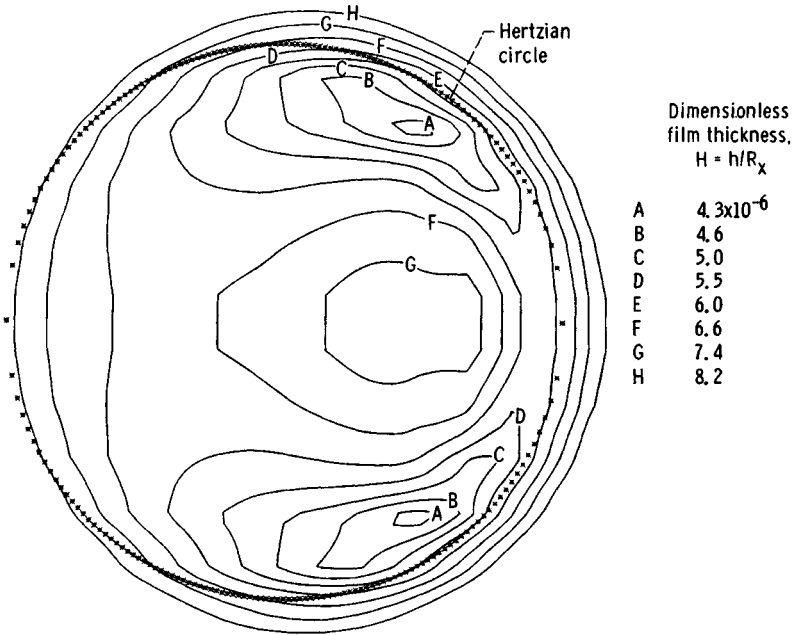
Fig. 21.71   Contour plot of dimensionless film thickness. $k = 1.25$; $U = 0.168 \times 10^{-11}$;
$W = 0.111 \times 10^{-6}$; $G = 4522$. (From Ref. 39.)

significant for soft-EHL results. The expression showing the effect of the ellipticity parameter is of exponential form in both equations, but with quite different constants.

A major difference between Eqs. (21.57) and (21.58) is the absence of the materials parameter in the expression for soft EHL. There are two reasons for this: one is the negligible effect of the relatively low pressures on the viscosity of the lubricating fluid, and the other is the way in which the role of elasticity is automatically incorporated into the prediction of conjunction behavior through the parameters U and W. Apparently the chief effect of elasticity is to allow the Hertzian contact zone to grow in response to increases in load.

21.3.5   Film Thickness for Different Regimes of Fluid-Film Lubrication

The types of lubrication that exist within nonconformal contacts like that shown in Fig. 21.70 are influenced by two major physical effects: the elastic deformation of the solids under an applied load and the increase in fluid viscosity with pressure. Therefore, it is possible to have four regimes of fluid-film lubrication, depending on the magnitude of these effects and on their relative importance. In this section because of the need to represent the four fluid-film lubrication regimes graphically, the dimensionless grouping presented in Section 21.3.2 will need to be recast. That is, the set of dimensionless parameters given in Section 21.3.2 {H, U, W, G, and k}—will be reduced by one parameter without any loss of generality. Thus the dimensionless groupings to be used here are:

Dimensionless film parameter

$$\hat{H} = H \left(\frac{W}{U}\right)^2 \tag{21.59}$$

Dimensionless viscosity parameter

$$g_v = \frac{GW^3}{U^2} \tag{21.60}$$

Dimensionless elasticity parameter

$$g_e = \frac{W^{8/3}}{U^2} \tag{21.61}$$

The ellipticity parameter remains as discussed in Section 21.3.1, Eq. (21.39). Therefore the reduced dimensionless group is $\{\hat{H}, g_v, g_e, k\}$.

Isoviscous-Rigid Regime

In this regime the magnitude of the elastic deformation of the surfaces is such an insignificant part of the thickness of the fluid film separating them that it can be neglected, and the maximum pressure in the contact is too low to increase fluid viscosity significantly. This form of lubrication is typically encountered in circular-arc thrust bearing pads; in industrial processes in which paint, emulsion, or protective coatings are applied to sheet or film materials passing between rollers; and in very lightly loaded rolling bearings.

The influence of conjunction geometry on the isothermal hydrodynamic film separating two rigid solids was investigated by Brewe et al.[42] The effect of geometry on the film thickness was determined by varying the radius ratio R_y/R_x from 1 (circular configuration) to 36 (a configuration approaching a rectangular contact). The film thickness was varied over two orders of magnitude for conditions representative of steel solids separated by a paraffinic mineral oil. It was found that the computed minimum film thickness had the same speed, viscosity, and load dependence as the classical Kapitza solution,[43] so that the new dimensionless film thickness H is constant. However, when the Reynolds cavitation condition ($\partial p / \partial n = 0$ and $p = 0$) was introduced at the cavitation boundary, where n represents the coordinate normal to the interface between the full film and the cavitation region, an additional geometrical effect emerged. According to Brewe et al.,[42] the dimensionless minimum-film-thickness parameter for the isoviscous-rigid regime should now be written as

$$(\hat{H}_{min})_{ir} = 128\alpha\lambda_b^2 \left[0.131 \tan^{-1}\left(\frac{\alpha}{2}\right) + 1.683 \right]^2 \tag{21.62}$$

where

$$\alpha = \frac{R_y}{R_x} \approx (k)^{\pi/2} \tag{21.63}$$

and

$$\lambda_b = \left(1 + \frac{2}{3\alpha} \right)^{-1} \tag{21.64}$$

In Eq. (21.62) the dimensionless film thickness parameter $\hat{H}$ is shown to be strictly a function only of the geometry of the contact described by the ratio $\alpha = R_y/R_x$.

Piezoviscous-Rigid Regime

If the pressure within the contact is sufficiently high to increase the fluid viscosity within the conjunction significantly, it may be necessary to consider the pressure–viscosity characteristics of the lubricant while assuming that the solids remain rigid. For the latter part of this assumption to be valid, it is necessary that the deformation of the surfaces remain an insignificant part of the fluid-film thickness. This form of lubrication may be encountered on roller end-guide flanges, in contacts in moderately loaded cylindrical tapered rollers, and between some piston rings and cylinder liners.

From Hamrock and Dowson[44] the minimum-film-thickness parameter for the piezoviscous-rigid regime can be written as

$$(\hat{H}_{min})_{pvr} = 1.66 \, g_v^{2/3} (1 - e^{-0.68k}) \tag{21.65}$$

Note the absence of the dimensionless elasticity parameter g_e from Eq. (21.65).

Isoviscous-Elastic (Soft-EHL) Regime

In this regime the elastic deformation of the solids is a significant part of the thickness of the fluid film separating them, but the pressure within the contact is quite low and insufficient to cause any substantial increase in viscosity. This situation arises with materials of low elastic modulus (such as rubber), and it is a form of lubrication that may be encountered in seals, human joints, tires, and elastomeric material machine elements.

If the film thickness equation for soft EHL [Eq. (21.58)] is rewritten in terms of the reduced dimensionless grouping, the minimum-film-thickness parameter for the isoviscous-elastic regime can be written as

$$(\hat{H}_{min})_{ie} = 8.70 \, g_e^{0.67} (1 - 0.85 e^{-0.31k}) \tag{21.66}$$

Note the absence of the dimensionless viscosity parameter g_v from Eq. (21.66).

Piezoviscous-Elastic (Hard-EHL) Regime

In fully developed elastohydrodynamic lubrication the elastic deformation of the solids is often a significant part of the thickness of the fluid film separating them, and the pressure within the contact is high enough to cause a significant increase in the viscosity of the lubricant. This form of lubrication is typically encountered in ball and roller bearings, gears, and cams.

Once the film thickness equation [Eq. (21.57)] has been rewritten in terms of the reduced dimensionless grouping, the minimum film parameter for the piezoviscous-elastic regime can be written as

$$(\hat{H}_{min})_{pve} = 3.42 \, g_v^{0.49} g_e^{0.17} \, (1 - e^{-0.68k}) \tag{21.67}$$

An interesting observation to make in comparing Eqs. (21.65) through (21.67) is that in each case the sum of the exponents on g_v and g_e is close to the value of $\frac{2}{3}$ required for complete dimensional representation of these three lubrication regimes: piezoviscous-rigid, isoviscous-elastic, and piezoviscous-elastic.

Contour Plots

Having expressed the dimensionless minimum-film-thickness parameter for the four fluid-film regimes in Eqs. (21.62) to (21.67), Hamrock and Dowson[44] used these relationships to develop a map of the lubrication regimes in the form of dimensionless minimum-film-thickness parameter contours. Some of these maps are shown in Figs. 21.72–21.74 on a log-log grid of the dimensionless viscosity and elasticity parameters for ellipticity parameters of 1, 3, and 6, respectively. The procedure used to obtain these figures can be found in Ref. 44. The four lubrication regimes are clearly shown in Figs. 21.72–21.74. By using these figures for given values of the parameters k, g_v, and g_e, the fluid-film lubrication regime in which any elliptical conjunction is operating can be ascertained and the approximate value of $\hat{H}_{min}$ can be determined. When the lubrication regime is known, a more accurate value of $\hat{H}_{min}$ can be obtained by using the appropriate dimensionless minimum-film-thickness equation. These results are particularly useful in initial investigations of many practical lubrication problems involving elliptical conjunctions.
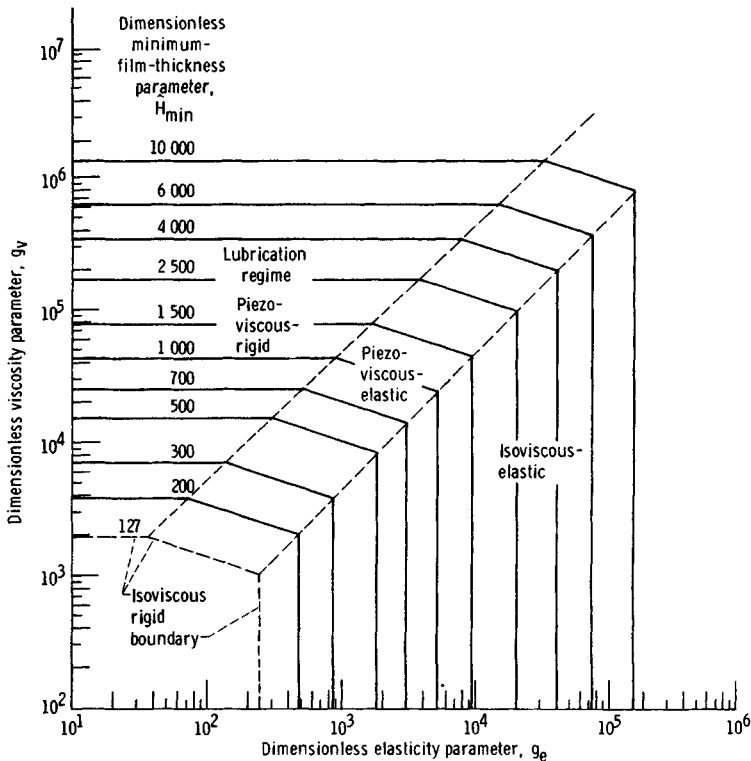
Fig. 21.72 Map of lubrication regimes for ellipticity parameter k of 1. (From Ref. 44.)
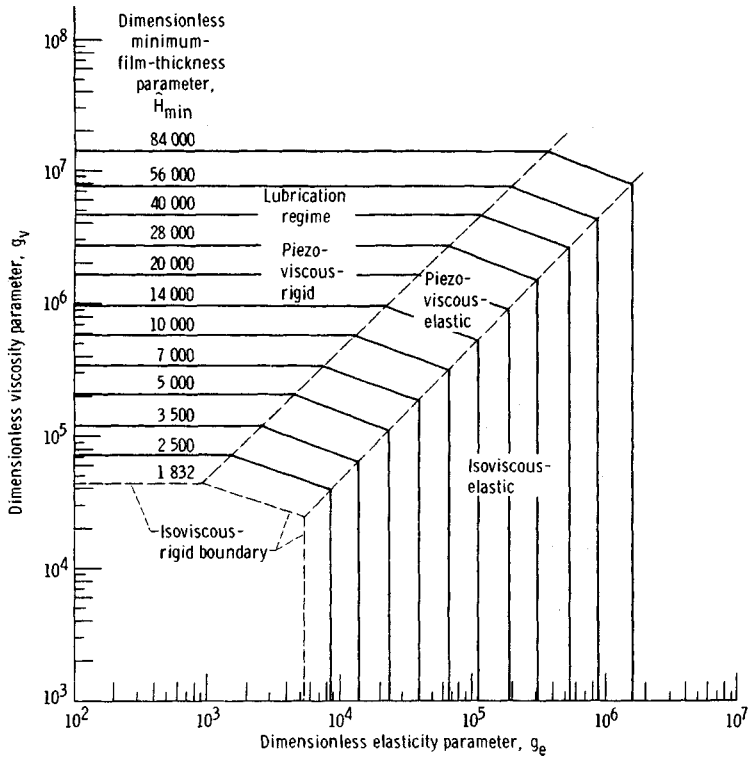
Fig. 21.73 Map of lubrication regimes for ellipticity parameter k of 3. (From Ref. 44.)

21.3.6 Rolling-Element Bearings

Rolling-element bearings are precision, yet simple, machine elements of great utility, whose mode of lubrication is elastohydrodynamic. This section describes the types of rolling-element bearings and their geometry, kinematics, load distribution, and fatigue life, and demonstrates how elastohydrodynamic lubrication theory can be applied to the operation of rolling-element bearings. This section makes extensive use of the work by Hamrock and Dowson[10] and by Hamrock and Anderson.[6]

Bearing Types

A great variety of both design and size range of ball and roller bearings is available to the designer. The intent of this section is not to duplicate the complete descriptions given in manufacturers' catalogs, but rather to present a guide a representative bearing types along with the approximate range of sizes available. Tables 21.9–21.17 illustrate some of the more widely used bearing types. In addition, there are numerous types of specialty bearings available for which space does not permit a complete cataloging. Size ranges are given in metric units. Traditionally, most rolling-element bearings have been manufactured to metric dimensions, predating the efforts toward a metric standard. In addition to bearing types and approximate size ranges available, Tables 21.9–21.17 also list approximate relative load-carrying capabilities, both radial and thrust, and, where relevant, approximate tolerances to misalignment.

Rolling bearings are an assembly of several parts–an inner race, an outer race, a set of balls or rollers, and a cage or separator. The cage or separator maintains even spacing of the rolling elements. A cageless bearing, in which the annulus is packed with the maximum rolling-element complement, is called a full-complement bearing. Full-complement bearings have high load capacity but lower speed limits than bearings equipped with cages. Tapered-roller bearings are an assembly of a cup, a cone, a set of tapered rollers, and a cage.

Ball Bearings.   Ball bearings are used in greater quantity than any other type of rolling bearing. For an application where the load is primarily radial with some thrust load present, one of the types in Table 21.9 can be chosen. A Conrad, or deep-groove, bearing has a ball complement limited by
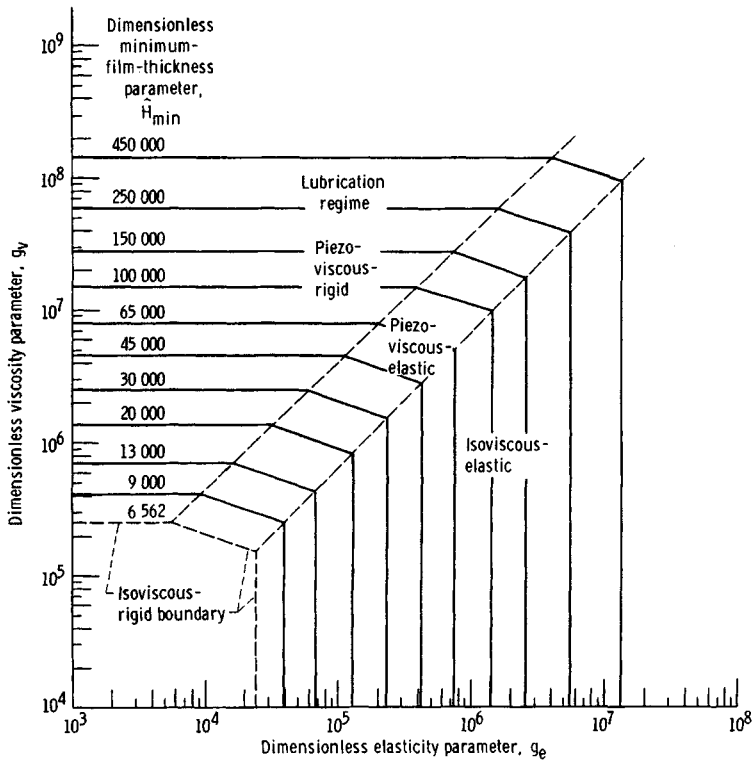
Fig. 21.74   Map of lubrication regimes for ellipticity parameter k of 6. (From Ref. 44.)

the number of balls that can be packed into the annulus between the inner and outer races with the inner race resting against the inside diameter of the outer race. A stamped and riveted two-piece cage, piloted on the ball set, or a machined two-piece cage, ball piloted or race piloted, is almost always used in a Conrad bearing. The only exception is a one-piece cage with open-sided pockets that is snapped into place. A filling-notch bearing has both inner and outer races notched so that a ball complement limited only by the annular space between the races can be used. It has low thrust capacity because of the filling notch.

The self-aligning internal bearing shown in Table 21.9 has an outer-race ball path ground in a spherical shape so that it can accept high levels of misalignment. The self-aligning external bearing has a multipiece outer race with a spherical interface. It too can accept high misalignment and has higher capacity than the self-aligning internal bearing. However, the external self-aligning bearing is somewhat less self-aligning than its internal counterpart because of friction in the multipiece outer race.

Representative angular-contact ball bearings are illustrated in Table 21.10. An angular-contact ball bearing has a two-shouldered ball groove in one race and a single-shouldered ball groove in the other race. Thus it is capable of supporting only a unidirectional thrust load. The cutaway shoulder allows assembly of the bearing by snapping over the ball set after it is positioned in the cage and outer race. This also permits use of a one-piece, machined, race-piloted cage that can be balanced for high-speed operation. Typical contact angles vary from 15° to 25°.

Angular-contact ball bearings are used in duplex pairs mounted either back to back or face to face as shown in Table 21.10. Duplex bearing pairs are manufactured so that they "preload" each other when clamped together in the housing and on the shaft. The use of preloading provides stiffer shaft support and helps prevent bearing skidding at light loads. Proper levels of preload can be obtained from the manufacturer. A duplex pair can support bidirectional thrust load. The back-to-back arrangement offers more resistance to moment or overturning loads than does the face-to-face arrangement.

Where thrust loads exceed the capability of a simple bearing, two bearings can be used in tandem, with both bearings supporting part of the thrust load. Three or more bearings are occasionally used

Table 21.9 Characteristics of Representative Radial Ball Bearings (From Ref. 10)

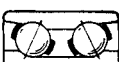| Type	Approximate Range of Bore Sizes, mm		Relative Capacity		Limiting Speed Factor	Tolerance to Misalignment
	Minimum	Maximum	Radial	Thrust		
Conrad or deep groove	3	1060	1.00	^{a}0.7	1.0	±0°15′
Maximum capacity or filling notch	10	130	1.2–1.4	^{a}0.2	1.0	±0°3′
Magneto or counterbored outer	3	200	0.9–1.3	^{b}0.5–0.9	1.0	±0°5′
Airframe or aircraft control	4.826	31.75	High static capacity	^{a}0.5	0.2	0°
Self-aligning, internal	5	120	0.7	^{b}0.2	1.0	±2°30′
Self-aligning, external	—	—	1.0	^{a}0.7	1.0	High
Double row, maximum	6	110	1.5	^{a}0.2	1.0	±0°3′
Double row, deep groove	6	110	1.5	^{a}1.4	1.0	0°

^{a}Two directions.
^{b}One direction.

in tandem, but this is discouraged because of the difficulty in achieving good load sharing. Even slight differences in operating temperature will cause a maldistribution of load sharing.

The split-ring bearing shown in Table 21.10 offers several advantages. The split ring (usually the inner) has its ball groove ground as a circular arc with a shim between the ring halves. The shim is then removed when the bearing is assembled so that the split-ring ball groove has the shape of a gothic arch. This reduces the axial play for a given radial play and results in more accurate axial positioning of the shaft. The bearing can support bidirectional thrust loads but must not be operated for prolonged periods of time at predominantly radial loads. This results in three-point ball–race contact and relatively high frictional losses. As with the conventional angular-contact bearing, a one-piece precision-machined cage is used.

Ball thrust bearings (90° contact angle), Table 21.11, are used almost exclusively for machinery with vertical oriented shafts. The flat-race bearing allows eccentricity of the fixed and rotating members. An additional bearing must be used for radial positioning. It has low load capacity because of the very small ball–race contacts and consequent high Hertzian stress. Grooved-race bearings have higher load capacities and are capable of supporting low-magnitude radial loads. All of the pure thrust ball bearings have modest speed capability because of the 90° contact angle and the consequent high level of ball spinning and frictional losses.

Roller Bearings. Cylindrical roller bearings, Table 21.12, provide purely radial load support in most applications. An N or U type of bearing will allow free axial movement of the shaft relative to the housing to accommodate differences in thermal growth. An F or J type of bearing will support a light thrust load in one direction; and a T type of bearing will support a light bidirectional thrust load.

Table 21.10   Characteristics of Representative Angular-Contact Ball Bearings (From Ref. 10)

Type		Approximate Range of Bore Sizes, mm		Relative Capacity		Limiting Speed Factor	Tolerance to Misalignment
		Minimum	Maximum	Radial	Thrust		
One-directional thrust		10	320	[b]1.00–1.15	[a,b]1.5–2.3	[b]1.1–3.0	±0°2′
Duplex, back to back		10	320	1.85	[c]1.5	3.0	0°
Duplex, face to face		10	320	1.85	[c]1.5	3.0	0°
Duplex, tandem		10	320	1.85	[a]2.4	3.0	0°
Two-directional or split ring		10	110	1.15	[c]1.5	3.0	±0°2′
Double row		10	140	1.5	[c]1.85	0.8	0°
Double row, maximum		10	110	1.65	[a]0.5 [d]1.5	0.7	0°

[a]One direction.
[b]Depends on contact angle.
[c]Two directions.
[d]In other direction.

Table 21.11   Characteristics of Representative Thrust Ball Bearings (From Ref. 10)

Type		Approximate Range of Bore Sizes, mm		Relative Capacity		Limiting Speed Factor	Tolerance to Misalignment
		Minimum	Maximum	Radial	Thrust		
One directional, flat race		6.45	88.9	0	[a]0.7	0.10	[b]0°
One directional, grooved race		6.45	1180	0	[a]1.5	0.30	0°
Two directional, grooved race		15	220	0	[c]1.5	0.30	0°

[a]One direction.
[b]Accepts eccentricity.
[c]Two directions.

Table 21.12 Characteristics of Representative Cylindrical Roller Bearings (From Ref. 10)

Type		Approximate Range of Bore Sizes, mm		Relative Capacity		Limiting Speed Factor	Tolerance to Misalignment
		Minimum	Maximum	Radial	Thrust		
Separable outer ring, nonlocating (RN, RIN)		10	320	1.55	0	1.20	±0°5′
Separable inner ring, nonlocating (RU, RIU)		12	500	1.55	0	1.20	±0°5′
Separable outer ring, one-direction locating (RF, RIF)		40	177.8	1.55	[a]Locating	1.15	±0°5′
Separable inner ring, one-direction locating (RJ, RIJ)		12	320	1.55	[a]Locating	1.15	±0°5′
Self-contained, two-direction locating		12	100	1.35	[b]Locating	1.15	±0°5′
Separable inner ring, two-direction locating (RT, RIT)		20	320	1.55	[b]Locating	1.15	±0°5′
Nonlocating, full complement (RK, RIK)		17	75	2.10	0	0.20	±0°5′
Double row, separable outer ring, nonlocating (RD)		30	1060	1.85	0	1.00	0°
Double row, separable inner ring, nonlocating		70	1060	1.85	0	1.00	0°

[a]One direction.
[b]Two directions.

Cylindrical roller bearings have moderately high radial load capacity as well as high-speed capability. Their speed capability exceeds that of either spherical or tapered-roller bearings. A commonly used bearing combination for support of a high-speed rotor is an angular-contact ball bearing or duplex pair and a cylindrical roller bearing.

As explained in the following section on bearing geometry, the rollers in cylindrical roller bearings are seldom pure cylinders. They are crowned or made slightly barrel shaped to relieve stress concentrations of the roller ends when any misalignment of the shaft and housing is present.

Cylindrical roller bearings may be equipped with one- or two-piece cages, usually race piloted. For greater load capacity, full-complement bearings can be used, but at a significant sacrifice in speed capability.

Table 21.13 Characteristics of Representative Spherical Roller Bearings (From Ref. 10)

Type		Approximate Range of Bore Sizes, mm		Relative Capacity		Limiting Speed Factor	Tolerance to Misalignment
		Minimum	Maximum	Radial	Thrust		
Single row, barrel or convex		20	320	2.10	0.20	0.50	±2°
Double row, barrel or convex		25	1250	2.40	0.70	0.50	±1°30′
Thrust		85	360	[a]0.10 [b]0.10	[a]1.80 [b]2.40	0.35–0.50	±3°
Double row, concave		50	130	2.40	0.70	0.50	±1°30′
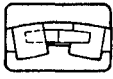
[a]Symmetric rollers.
[b]Asymmetric rollers.

Spherical roller bearings, Tables 21.13–21.15, are made as either single- or double-row bearings. The more popular bearing design uses barrel-shaped rollers. An alternative design employs hourglass-shaped rollers. Spherical roller bearings combine very high radial load capacity with modest thrust load capacity (with the exception of the thrust type) and excellent tolerance to misalignment. They find widespread use in heavy-duty rolling mill and industrial gear drives, where all of these bearing characteristics are requisite.

Tapered-roller bearings, Table 21.16, are also made as single- or double-row bearings with combinations of one- or two-piece cups and cones. A four-row bearing assembly with two- or three-piece cups and cones is also available. Bearings are made with either a standard angle for applications in which moderate thrust loads are present or with a steep angle for high thrust capacity. Standard and special cages are available to suit the application requirements.

Single-row tapered-roller bearings must be used in pairs because a radially loaded bearing generates a thrust reaction that must be taken by a second bearing. Tapered-roller bearings are normally set up with spacers designed so that they operate with some internal play. Manufacturers' engineering journals should be consulted for proper setup procedures.

Needle roller bearings, Table 21.17, are characterized by compactness in the radial direction and are frequently used without an inner race. In the latter case the shaft is hardened and ground to serve

Table 21.14 Characteristics of Standardized Double-Row, Spherical Roller Bearings (From Ref. 10)

Type		Roller Design	Retainer Design	Roller Guidance	Roller-race Contact
SLB		Symmetric	Machined, roller piloted	Retainer pockets	Modified line, both races
SC		Symmetric	Stamped, race piloted	Floating guide ring	Modified line, both races
SD		Asymmetric	Machined, race piloted	Inner-ring center rib	Line contact, outer; point contact, inner

Table 21.15 Characteristics of Spherical Roller Bearings (From Ref. 10)

Series	Types	Approximate Range of Bore Sizes, mm		Approximate Relative Capacity[a]		Limiting Speed Factor
		Minimum	Maximum	Radial	Thrust	
202	Single-row barrel	20	320	1.0	0.11	0.5
203	Single-row barrel	20	240	1.7	.18	.5
204	Single-row barrel	25	110	2.1	.22	.4
212	SLB	35	75	1.0	.26	.6
213	SLB	30	70	1.7	.53	
22, 22K	SLB, SC, SD	30	320	1.7	.46	
23, 23K	SLB, SC, SD	40	280	2.7	1.0	
30, 30K	SLB, SC, SD	120	1250	1.2	.29	.7
31, 31K	SLB, SC, SD	110	1250	1.7	.54	.6
32, 32K	SLB, SC, SD	100	850	2.1	.78	.6
39, 39K	SD	120	1250	.7	.18	.7
40, 40K	SD	180	250	1.5	—	.7

[a]Load capacities are comparative within the various series of spherical roller bearings only. For a given envelope size, a spherical roller bearing has a radial capacity approximately equal to that of a cylindrical roller bearing.

as the inner race. Drawn cups, both open and closed end, are frequently used for grease retention. Drawn cups are thin walled and require substantial support from the housing. Heavy-duty roller bearings have relatively rigid races and are more akin to cylindrical roller bearings with long-length-to-diameter-ratio rollers.

Needle roller bearings are more speed limited than cylindrical roller bearings because of roller skewing at high speeds. A high percentage of needle roller bearings are full-complement bearings. Relative to a caged needle bearing, these have higher load capacity but lower speed capability.

There are many types of specialty bearings available other than those discussed here. Aircraft bearings for control systems, thin-section bearings, and fractured-ring bearings are some of the more widely used bearings among the many types manufactured. A complete coverage of all bearing types is beyond the scope of this chapter.

Angular-contact ball bearings and cylindrical roller bearings are generally considered to have the highest speed capabilities. Speed limits of roller bearings are discussed in conjunction with lubrication methods. The lubrication system employed has as great an influence on limiting bearing speed as does the bearing design.

Geometry

The operating characteristics of a rolling-element bearing depend greatly on the diametral clearance of the bearing. This clearance varies for the different types of bearings discussed in the preceding section. In this section, the principal geometrical relationships governing the operation of unloaded rolling-element bearings are developed. This information will be of vital interest when such quantities as stress, deflection, load capacity, and life are considered in subsequent sections. Although bearings rarely operate in the unloaded state, an understanding of this section is vital to the appreciation of the remaining sections.

Geometry of Ball Bearings

Pitch Diameter and Clearance. The cross section through a radial, single-row ball bearing shown in Fig. 21.75 depicts the radial clearance and various diameters. The pitch diameter d_e is the mean of the inner- and outer-race contact diameters and is given by

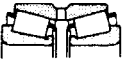$$d_e = d_i + \tfrac{1}{2}(d_o - d_i) \quad \text{or} \quad d_e = \tfrac{1}{2}(d_o + d_i) \tag{21.68}$$

Also from Fig. 21.75, the diametral clearance denoted by P_d can be written as

$$P_d = d_o - d_i - 2d \tag{21.69}$$

Diametral clearance may therefore be thought of as the maximum distance that one race can move diametrally with respect to the other when no measurable force is applied and both races lie in the

Table 21.16 Characteristics of Representative Tapered Roller Bearings (From Ref. 10)

Type		Subtype	Approximate Range of Bore Sizes, mm	
			Minimum	Maximum
Single row (TS)		TST—Tapered bore	8	1690
		TSS—Steep angle	24	430
		TS—Pin cage	16	1270
		TSE, TSK—keyway cones	—	
		TSF, TSSF—flanged cup	12	380
		TSG—steering gear (without cone)	8	1070
			—	
Two row, double cone, single cups (TDI)		TDIK, TDIT,	30	1200
		TDITP—tapered bore	30	860
		TDIE, TDIKE—slotted	24	690
		double cone	55	520
		TDIS—steep angle		
Two row, double cup, single cones, adjustable (TDO)		TDO	8	1830
		TDOS—steep angle	20	1430
Two row, double cup, single cones, nonadjustabe (TNA)		TNA	20	60
		TNASW—slotted cones	30	260
		TNASWE—extended cone rib	20	305
			8	70
		TNASWH—slotted cones, sealed	—	—
		TNADA, TNHDADX—self-aligning cup AD		
Four row, cup adjusted (TQO)			70	1500
		TQO, TQOT—tapered bore	250	1500
Four row cup adjusted (TQI)		TQIT—tapered bore	—	—

same plane. Although diametral clearance is generally used in connection with single-row radial bearings, Eq. (21.69) is also applicable to angular-contact bearings.
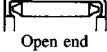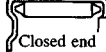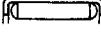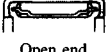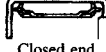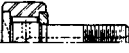
Race Conformity. Race conformity is a measure of the geometrical conformity of the race and the ball in a plane passing through the bearing axis, which is a line passing through the center of the bearing perpendicular to its plane and transverse to the race. Figure 21.76 is a cross section of a ball bearing showing race conformity, expressed as

$$f = \frac{r}{d} \tag{21.70}$$

For perfect conformity, where the radius of the race is equal to the ball radius, f is equal to ½. The closer the race conforms to the ball, the greater the frictional heat within the contact. On the other hand, open-race curvature and reduced geometrical conformity, which reduce friction, also increase the maximum contact stresses and, consequently, reduce the bearing fatigue life. For this reason, most ball bearings made today have race conformity ratios in the range $0.51 \leq f \leq 0.54$, with $f = 0.52$ being the most common value. The race conformity ratio for the outer race is usually made slightly larger than that for the inner race to compensate for the closer conformity in the plane of the bearing between the outer race and ball than between the inner race and ball. This tends to equalize the contact stresses at the inner- and outer-race contacts. The difference in race conformities does not normally exceed 0.02.

Contact Angle. Radial bearings have some axial play since they are generally designed to have a diametral clearance, as shown in Fig. 21.77. This implies a free-contact angle different from zero. Angular-contact bearings are specifically designed to operate under thrust loads. The clearance built

Table 21.17 Characteristics of Representative Needle Roller Bearings (From Ref. 10)

Type		Bore Sizes, mm		Relative Load Capacity		Limiting Speed Factor	Misalignment Tolerance
		Minimum	Maximum	Dynamic	Static		
Drawn cup, needle	Open end Closed end	3	185	High	Moderate	0.3	Low
Drawn cup, needle, grease retained		4	25	High	Moderate	0.3	Low
Drawn cup, roller	Open end Closed end	5	70	Moderate	Moderate	0.9	Moderate
Heavy-duty roller		16	235	Very high	Moderate	1.0	Moderate
Caged roller		12	100	Very high	High	1.0	Moderate
Cam follower		12	150	Moderate to high	Moderate to high	0.3–0.9	Low
Needle thrust		6	105	Very high	Very high	0.7	Low

into the unloaded bearing, along with the race conformity ratio, determines the bearing free-contact angle. Figure 21.77 shows a radial bearing with contact due to the axial shift of the inner and outer races when no measurable force is applied.

Before the free-contact angle is discussed, it is important to define the distance between the centers of curvature of the two races in line with the center of the ball in both Figs. 21.77a and 21.77b. This distance—denoted by x in Fig. 21.77a and by D in Fig. 21.77b—depends on race radius and ball diameter. Denoting quantities referred to the inner and outer races by subscripts i and o, respectively, we see from Figs. 21.77a and 21.77b that
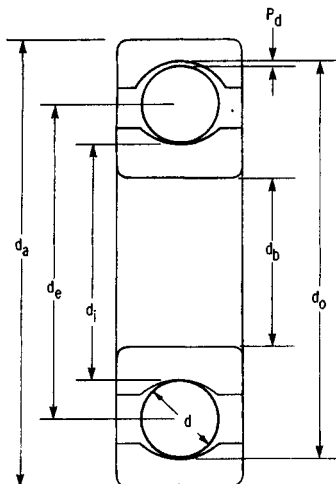
Fig. 21.75 Cross section through radial, single-row ball bearing. (From Ref. 10.)
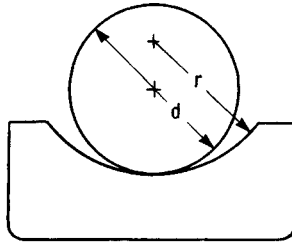
Fig. 21.76 Cross section of ball and outer race, showing race conformity. (From Ref. 10.)

$$\frac{P_d}{4} + d + \frac{P_d}{4} = r_o - x + r_i$$

or

$$x = r_o + r_i - d - \frac{P_d}{2}$$

and

$$d = r_o - D + r_i$$

or

$$D = r_o + r_i - d \qquad (21.71)$$

From these equations, we can write

$$x = D - \frac{P_d}{2}$$

This distance, shown in Fig. 21.77, will be useful in defining the contact angle.
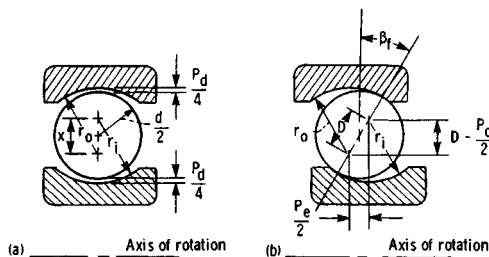By using Eq. (21.70), we can write Eq. (21.71) as

$$D = Bd \qquad (21.72)$$

where

$$B = f_o + f_i - 1 \qquad (21.73)$$

The quantity B in Eq. (21.72) is known as the total conformity ratio and is a measure of the combined

Fig. 21.77 Cross section of radial ball bearing, showing ball–race contact due to axial shift of inner and outer rings. (From Ref. 10.) (a) Initial position. (b) Shifted position.

conformity of both the outer and inner races to the ball. Calculations of bearing deflection in later sections depend on the quantity B.

The free-contact angle β_f (Fig. 21.77) is defined as the angle made by a line through the points of contact of the ball and both races with a plane perpendicular to the bearing axis of rotation when no measurable force is applied. Note that the centers of curvature of both the outer and inner races lie on the line defining the free-contact angle. From Fig. 21.77, the expression for the free-contact angle can be written as

$$\cos \beta_f = \frac{D - P_d/2}{D} \tag{21.74}$$

By using Eqs. (21.69) and (21.71), we can write Eq. (21.74) as

$$\beta_f = \cos^{-1} \left[\frac{r_o + r_i - \frac{1}{2}(d_o - d_i)}{r_o + r_i - d} \right] \tag{21.75}$$

Equation (21.75) shows that if the size of the balls is increased and everything else remains constant, the free-contact angle is decreased. Similarly, if the ball size is decreased, the free-contact angle is increased.

From Eq. (21.74) the diametral clearance P_d can be written as

$$P_d = 2D(1 - \cos \beta_f) \tag{21.76}$$

This is an alternative definition of the diametral clearance given in Eq. (21.69).

Endplay. Free endplay P_e is the maximum axial movement of the inner race with respect to the outer race when both races are coaxially centered and no measurable force is applied. Free endplay depends on total curvature and contact angle, as shown in Fig. 21.77, and can be written as

$$P_e = 2D \sin \beta_f \tag{21.77}$$

The variation of free-contact angle and free endplay with the ratio $P_d/2d$ is shown in Fig. 21.78 for
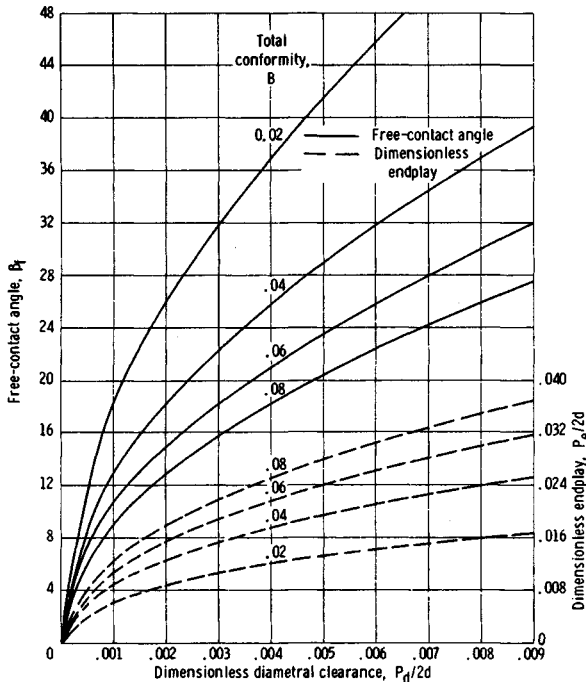
Fig. 21.78   Chart for determining free-contact angle and endplay. (From Ref. 10.)

Fig. 21.79 Shoulder height in ball bearing. (From Ref. 10.)

four values of total conformity normally found in single-row ball bearings. Eliminating β_f in Eqs. (21.76) and (21.77) enables the establishment of the following relationships between free endplay and diametral clearance:

$$P_d = 2D - [(2D)^2 - P_c^2]^{1/2}$$

$$P_e = (4DP_d - P_d^2)^{1/2}$$
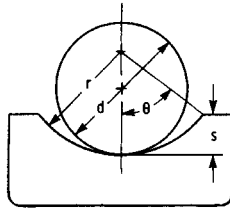
Shoulder Height. The shoulder height of ball bearings is illustrated in Fig. 21.79. Shoulder height, or race depth, is the depth of the race groove measured from the shoulder to the bottom of the groove and is denoted by s in Fig. 21.79. From this figure the equation defining the shoulder height can be written as

$$s = r(1 - \cos \theta) \qquad (21.78)$$

The maximum possible diametral clearance for complete retention of the ball–race contact within the race under zero thrust load is given by

$$(P_d)_{\text{max}} = \frac{2Ds}{r}$$

Curvature Sum and Difference. A cross section of a ball bearing operating at a contact angle β is shown in Fig. 21.80. Equivalent radii of curvature for both inner- and outer-race contacts in, and normal to, the direction of rolling can be calculated from this figure. The radii of curvature for the ball–inner-race contact are

$$r_{ax} = r_{ay} = \frac{d}{2} \qquad (21.79)$$

$$r_{bx} = \frac{d_c - d \cos \beta}{2 \cos \beta} \qquad (21.80)$$

$$r_{by} = -f_i d = -r_i \qquad (21.81)$$

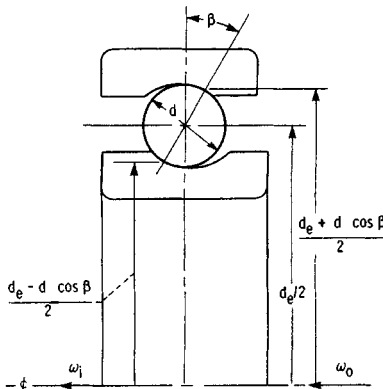The radii of curvature for the ball–outer-race contact are

Fig. 21.80 Cross section of ball bearing. (From Ref. 10.)

$$r_{ax} = r_{ay} = \frac{d}{2} \qquad (21.82)$$

$$r_{bx} = \frac{d_c + d \cos \beta}{2 \cos \beta} \qquad (21.83)$$

$$r_{by} = -f_o d = -r_o \qquad (21.84)$$

In Eqs. (21.80) and (21.81), β is used instead of β_f since these equations are also valid when a load is applied to the contact. By setting $\beta = 0°$, Eqs. (21.79)–(21.84) are equally valid for radial ball bearings. For thrust ball bearings, $r_{bx} = \infty$ and the other radii are defined as given in the preceding equations.

Equations (21.36) and (21.37) effectively redefine the problem of two ellipsoidal solids approaching one another in terms of an equivalent ellipsoidal solid of radii R_x and R_y approaching a plane. From the radius-of-curvature expressions, the radii R_x and R_y for the contact example discussed earlier can be written for the ball–inner-race contact as

$$R_x = \frac{d(d_e - d \cos \beta)}{2d_e} \qquad (21.85)$$

$$R_y = \frac{f_i d}{2f_i - 1} \qquad (21.86)$$

and for the ball–outer-race contact as

$$R_x = \frac{d(d_e + d \cos \beta)}{2d_e} \qquad (21.87)$$

$$R_y = \frac{f_o d}{2f_o - 1} \qquad (21.88)$$

Roller Bearings.   The equations developed for the pitch diameter d_e and diametral clearance P_d for ball bearings in Eqs. (21.68) and (21.69), respectively, are directly applicable for roller bearings.

Crowning.   To prevent high stresses at the edges of the rollers in cylindrical roller bearings, the rollers are usually crowned as shown in Fig. 21.81. A fully crowned roller is shown in Fig. 21.81a and a partially crowned roller in Fig. 21.81b. In this figure the crown curvature is greatly exaggerated for clarity. The crowning of rollers also gives the bearing protection against the effects of slight misalignment. For cylindrical rollers, $r_{ay}/d \approx 10^2$. In contrast, for spherical rollers in spherical roller bearings, as shown in Fig. 21.81, $r_{ay}/d \approx 4$. In Fig. 21.81 it is observed that the roller effective length l_r is the length presumed to be in contact with the races under loading. Generally, the roller effective length can be written as

$$l_r = l_t - 2r_c$$

where r_c is the roller corner radius or the grinding undercut, whichever is larger.
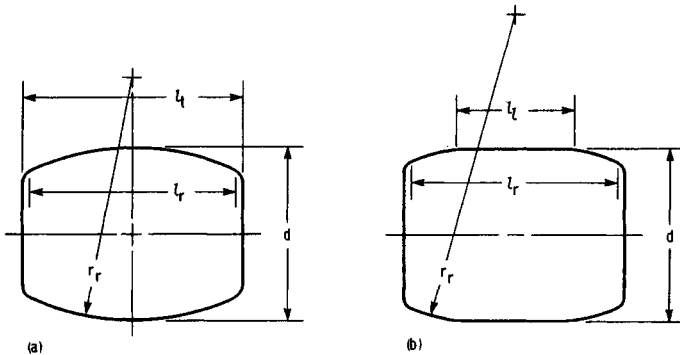
Fig. 21.81   Spherical and cylindrical rollers. (From Ref. 6.) (a) Spherical roller (fully crowned). (b) Cylindrical roller (partially crowned).

Race Conformity. Race conformity applies to roller bearings much as it applies to ball bearings. It is a measure of the geometrical conformity of the race and the roller. Figure 21.82 shows a cross section of a spherical roller bearing. From this figure the race conformity can be written as

$$f = \frac{r}{2r_{ay}}$$

In this equation if subscripts i or o are added to f and r, we obtain the values for the race conformity for the inner- and outer-race contacts.

Free Endplay and Contact Angle. Cylindrical roller bearings have a contact angle of zero and may take thrust load only by virtue of axial flanges. Tapered-roller bearings must be subjected to a thrust load or the inner and outer races (the cone and cup) will not remain assembled; therefore, tapered-roller bearings do not exhibit free diametral play. Radial spherical roller bearings are, however, normally assembled with free diametral play and, hence, exhibit free endplay. The diametral play P_d for a spherical roller bearing is the same as that obtained for ball bearings as expressed in Eq. (21.69). This diametral play as well as endplay is shown in Fig. 21.83 for a spherical roller bearing. From this figure we can write that

$$r_o \cos \beta = \left(r_o - \frac{P_d}{2} \right) \cos \gamma$$

or

$$\beta = \cos^{-1} \left[\left(1 - \frac{P_d}{2r_o} \right) \cos \gamma \right]$$

Also from Fig. 21.83 the free endplay can be written as
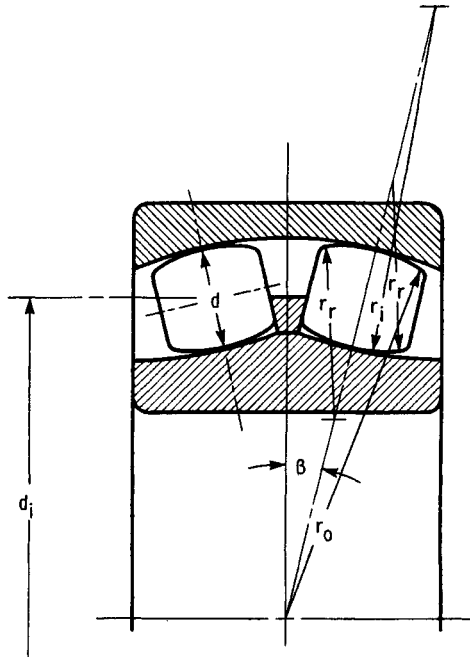
$$P_c = 2r_o(\sin \beta - \sin \gamma) + P_d \sin \gamma$$

Fig. 21.82 Spherical roller bearing geometry. (From Ref. 6.)
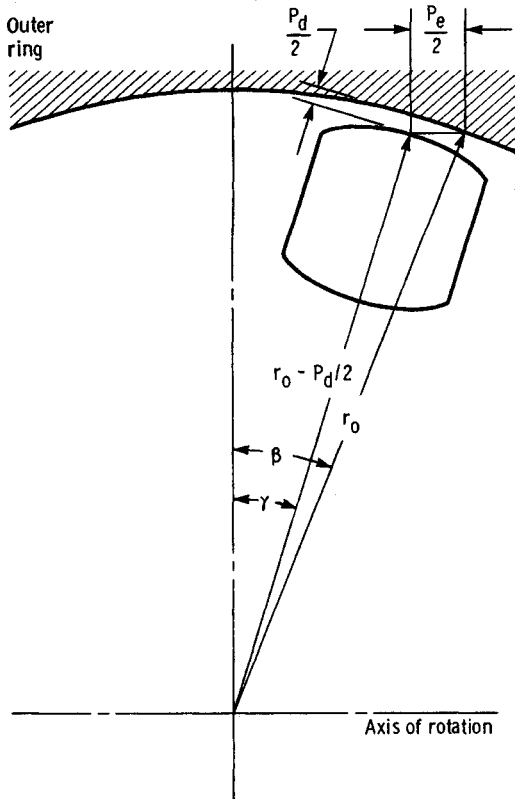
Fig. 21.83 Schematic diagram of spherical roller bearing, showing diametral play and endplay. (From Ref. 6.)

Curvature Sum and Difference. The same procedure will be used for defining the curvature sum and difference for roller bearings as was used for ball bearings. For spherical roller bearings, as shown in Fig. 21.82, the radii of curvature for the roller–inner-race contact can be written as

$$r_{ax} = \frac{d}{2}, \qquad r_{ay} = f_i \left(\frac{r_i}{2} \right)$$

$$r_{bx} = \frac{d_e - d \cos \beta}{2 \cos \beta}, \qquad r_{by} = -2 f_i r_{ay}$$

For the spherical roller bearing shown in Fig. 21.82 the radii of curvature for the roller–outer-race contact can be written as

$$r_{ax} = \frac{d}{2}, \qquad r_{ay} = f_o \left(\frac{r_o}{2} \right)$$

$$r_{bx} = -\frac{d_e + d \cos \beta}{2 \cos \beta}, \qquad r_{by} = -2 f_o r_{ay}$$

Knowing the radii of curvature for the contact condition, we can write the curvature sum and difference directly from Eqs. (21.34) and (21.35). Furthermore, the radius-of-curvature expressions R_x and R_y for spherical roller bearings can be written for the roller–inner-race contact as

$$R_x = \frac{d(d_c - d \cos \beta)}{2d_c} \tag{21.89}$$

$$R_y = \frac{2r_{ay}f_i}{2f_i - 1} \tag{21.90}$$

and for the roller–outer-race contact as

$$R_x = \frac{d(d_c + d \cos \beta)}{2d_c} \tag{21.91}$$

$$R_y = \frac{2r_{ay}f_o}{2f_o - 1} \tag{21.92}$$

Kinematics

The relative motions of the separator, the balls or rollers, and the races of rolling-element bearings are important to understanding their performance. The relative velocities in a ball bearing are somewhat more complex than those in roller bearings, the latter being analogous to the specialized case of a zero- or fixed-value contact-angle ball bearing. For that reason the ball bearing is used as an example here to develop approximate expressions for relative velocities. These are useful for rapid but reasonably accurate calculation of elastohydrodynamic film thickness, which can be used with surface roughnesses to calculate the lubrication life factor.

When a ball bearing operates at high speeds, the centrifugal force acting on the ball creates a difference between the inner- and outer-race contact angles, as shown in Fig. 21.84, in order to maintain force equilibrium on the ball. For the most general case of rolling and spinning at both inner- and outer-race contacts, the rolling and spinning velocities of the ball are as shown in Fig. 21.85.

The equations for ball and separator angular velocity for all combinations of inner- and outer-race rotation were developed by Jones.[45] Without introducing additional relationships to describe the elastohydrodynamic conditions at both ball–race contacts, however, the ball–spin-axis orientation angle ϕ cannot be obtained. As mentioned, this requires a long numerical solution except for the two extreme cases of outer- or inner-race control. These are illustrated in Fig. 21.86.

Race control assumes that pure rolling occurs at the controlling race, with all of the ball spin occurring at the other race contact. The orientation of the ball rotational axis is then easily determinable from bearing geometry. Race control probably occurs only in dry bearings or dry-film-lubricated bearings where Coulomb friction conditions exist in the ball–race contact ellipses. Pure rolling will occur at the race contact with the higher magnitude spin-opposing moment. This is usually the inner race at low speeds and the outer race at high speeds.
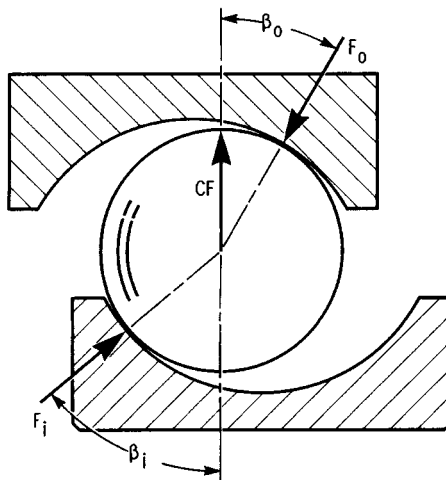

Fig. 21.84 Contact angles in a ball bearing at appreciable speeds. (From Ref. 6.)
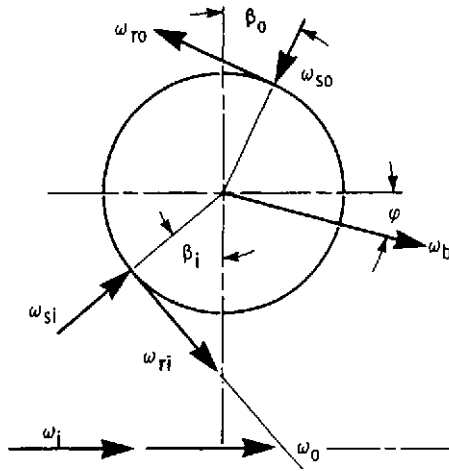
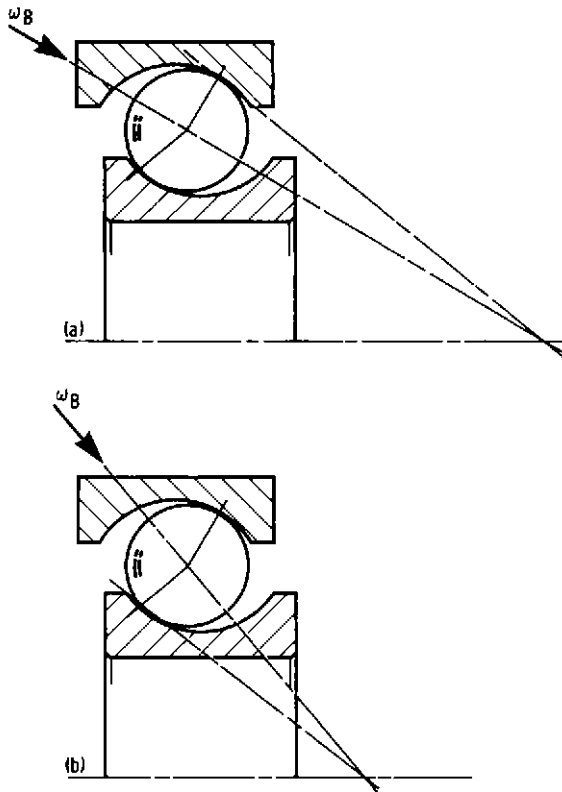**Fig. 21.85**   Angular velocities of a ball. (From Ref. 6.)

Fig. 21.86   Ball spin axis orientations for outer- and inner-race control. (From Ref. 6.) (a) Outer-race control. (b) Inner-race control.

In oil-lubricated bearings in which elastohydrodynamic films exist in both ball–race contacts, rolling with spin occurs at both contacts. Therefore, precise ball motions can only be determined through use of a computer analysis. We can approximate the situation with a reasonable degree of accuracy, however, by assuming that the ball rolling axis is normal to the line drawn through the centers of the two ball–race contacts. This is shown in Fig. 21.80.

The angular velocity of the separator or ball set ω_c about the shaft axis can be shown to be

$$\omega_c = \frac{(v_i + v_o)/2}{d_e/2}$$

$$= \frac{1}{2}\left[\omega_i\left(1 - \frac{d\cos\beta}{d_e}\right) + \omega_o\left(1 + \frac{d\cos\beta}{d_e}\right)\right] \tag{21.93}$$

where v_i and v_o are the linear velocities of the inner and outer contacts. The angular velocity of a ball ω_b about its own axis is

$$\omega_b = \frac{v_i - v_o}{d_e/2}$$

$$= \frac{d_e}{2d}\left[\omega_i\left(1 - \frac{d\cos\beta}{d_e}\right) - \omega_o\left(1 + \frac{d\cos\beta}{d_e}\right)\right] \tag{21.94}$$

To calculate the velocities of the ball–race contacts, which are required for calculating elastohydrodynamic film thicknesses, it is convenient to use a coordinate system that rotates at ω_c. This fixes the ball–race contacts relative to the observer. In the rotating coordinate system the angular velocities of the inner and outer races become

$$\omega_{ir} = \omega_i - \omega_c = \left(\frac{\omega_i - \omega_o}{2}\right)\left(1 + \frac{d\cos\beta}{d_e}\right)$$

$$\omega_{or} = \omega_o - \omega_c = \left(\frac{\omega_o - \omega_i}{2}\right)\left(1 - \frac{d\cos\beta}{d_e}\right)$$

The surface velocities entering the ball–inner-race contact for pure rolling are

$$u_{ai} = u_{bi} = \left(\frac{d_e - d\cos\beta}{2}\right)\omega_{ir} \tag{21.95}$$

or

$$u_{ai} = u_{bi} = \frac{d_e(\omega_i - \omega_o)}{4}\left(1 - \frac{d^2\cos^2\beta}{d_e^2}\right) \tag{21.96}$$

and those at the ball–outer-race contact are

$$u_{ao} = u_{bo} = \left(\frac{d_e + d\cos\beta}{2}\right)\omega_{or}$$

or

$$u_{ao} = u_{bo} = \frac{d_e(\omega_o - \omega_i)}{4}\left(1 - \frac{d^2\cos^2\beta}{d_e^2}\right) \tag{21.97}$$

For a cylindrical roller bearing $\beta = 0°$ and Eqs. (21.92), (21.94), (21.96), and (21.97) become, if d is roller diameter,

$$\omega_c = \frac{1}{2}\left[\omega_i\left(1 - \frac{d}{d_e}\right) + \omega_o\left(1 + \frac{d}{d_e}\right)\right]$$

$$\omega_R = \frac{d_e}{2d}\left[\omega_i\left(1 - \frac{d}{d_e}\right) + \omega_o\left(1 + \frac{d}{d_e}\right)\right]$$

$$u_{ai} = u_{bi} = \frac{d_e(\omega_i - \omega_o)}{4}\left(1 - \frac{d^2}{d_e^2}\right) \tag{21.98}$$

$$u_{ao} = u_{bo} = \frac{d_e(\omega_o - \omega_i)}{4}\left(1 - \frac{d^2}{d_e^2}\right)$$

For a tapered-roller bearing, equations directly analogous to those for a ball bearing can be used if d is the average diameter of the tapered roller, d_e is the diameter at which the geometric center of the rollers is located, and ω is the angle as shown in Fig. 21.87.

Static Load Distribution

Having defined a simple analytical expression for the deformation in terms of load in Section 21.3.1, it is possible to consider how the bearing load is distributed among the rolling elements. Most rolling-element bearing applications involve steady-state rotation of either the inner or outer race or both; however, the speeds of rotation are usually not so great as to cause ball or roller centrifugal forces or gyroscopic moments of significant magnitudes. In analyzing the loading distribution on the rolling elements, it is usually satisfactory to ignore these effects in most applications. In this section the load–deflection relationships for ball and roller bearings are given, along with radial and thrust load distributions of statically loaded rolling elements.

Load–Deflection Relationships. For an elliptical contact the load–deflection relationship given in Eq. (21.45) can be written as

$$F = K_{1.5}\delta^{3/2} \tag{21.99}$$

where

$$K_{1.5} = \pi k E'\left(\frac{2\delta R}{9\mathcal{F}^3}\right)^{1/2} \tag{21.100}$$

Similarly for a rectangular contact, Eq. (21.50) gives
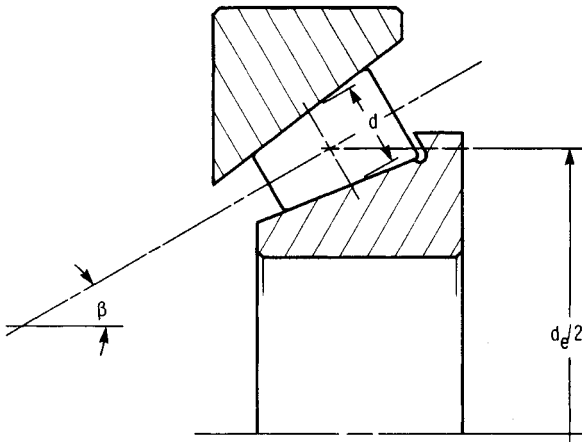
$$F = K_1\delta$$

where

Fig. 21.87 Simplified geometry for tapered-roller bearing. (From Ref. 6.)

$$K_1 = \left(\frac{\pi l E'}{2}\right)\left[\frac{1}{\tfrac{2}{3} + \ln(2r_{ax}/b) + \ln(2r_{bx}/b)}\right] \tag{21.101}$$

In general, then,

$$F = K_j\delta^j \tag{21.102}$$

in which $j = 1.5$ for ball bearings and 1.0 for roller bearings. The total normal approach between two races separated by a rolling element is the sum of the deformations under load between the rolling element and both races. Therefore

$$\delta = \delta_o + \delta_i \tag{21.103}$$

where

$$\delta_o = \left[\frac{F}{(K_j)_o}\right]^{1/j} \tag{21.104}$$

$$\delta_i = \left[\frac{F}{(K_j)_i}\right]^{1/j} \tag{21.105}$$

Substituting Eqs. (21.103)–(21.105) into Eq. (21.102) gives

$$K_j = \frac{1}{\{[1/(K_j)_o]^{1/j} + [1/(K_j)_i]^{1/j}\}^j}$$

Recall that $(K_j)_o$ and $(K_j)_i$ are defined by Eq. (21.100) or (21.101) for an elliptical or rectangular contact, respectively. From these equations we observe that $(K_j)_o$ and $(K_j)_i$ are functions of only the geometry of the contact and the material properties. The radial and thrust load analyses are presented in the following two sections and are directly applicable for radially loaded ball and roller bearings and thrust-loaded ball bearings.

Radially Loaded Ball and Roller Bearings.   A radially loaded rolling element with radial clearance P_d is shown in Fig. 21.88. In the concentric position shown in Fig. 21.88a, a uniform radial clearance between the rolling element and the races of $P_d/2$ is evident. The application of a small radial load to the shaft causes the inner race to move a distance $P_d/2$ before contact is made between a rolling element located on the load line and the inner and outer races. At any angle there will still be a radial clearance c that, if P_d is small compared with the radius of the tracks, can be expressed with adequate accuracy by

$$c = (1 - \cos \psi)\, P_d/2$$

On the load line where $\psi = 0$ the clearance is zero, but when $\psi = 90°$, the clearance retains its initial value of $P_d/2$.

The application of further load will cause elastic deformation of the balls and the elimination of clearance around an arc $2\psi_c$. If the interference or total elastic compression on the load is δ_{max}, the corresponding elastic compression of the ball δ_ψ along a radius at angle ψ to the load line will be given by

$$\delta_\psi = (\delta_{max} \cos \psi - c) = (\delta_{max} + P_d/2) \cos \psi - P_d/2$$

This assumes that the races are rigid. Now, it is clear from Fig. 21.88 that $(\delta_{max} + P_d/2)$ represents the total relative radial displacement of the inner and outer races. Hence,

$$\delta_\psi = \delta \cos \psi - P_d/2 \tag{21.106}$$

The relationship between load and elastic compression along the radius at angle ψ to the load vector is given by Eq. (21.102) as

$$F_\psi = K_j\delta_\psi^j$$

Substituting Eq. (21.106) into this equation gives

$$F_\psi = K_j(\delta \cos \psi - P_d/2)^j$$
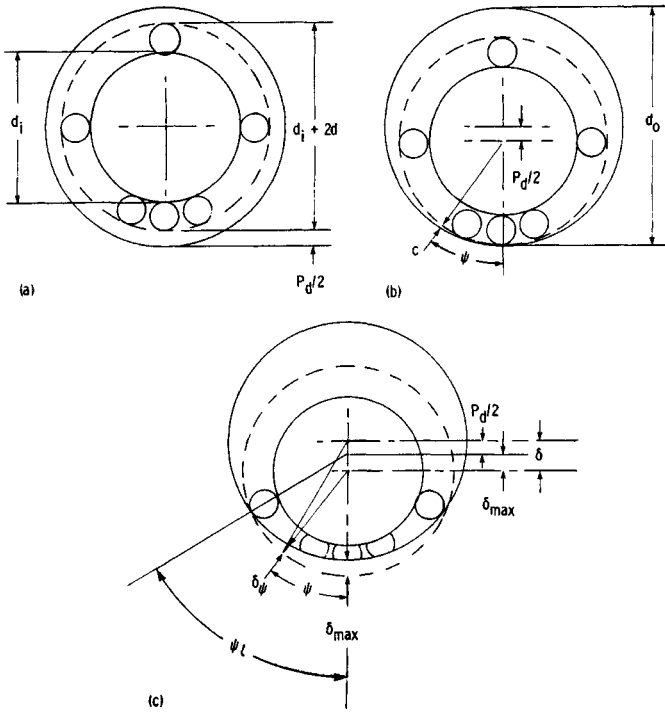
Fig. 21.88 Radially loaded rolling-element bearing. (From Ref. 10.) (a) Concentric arrangement. (b) Initial contact. (c) Interference.

For static equilibrium the applied load must equal the sum of the components of the rolling-element loads parallel to the direction of the applied load:

$$F_r = \sum F_\psi \cos \psi$$

Therefore

$$F_r = K_j \sum \left(\delta \cos \psi - \frac{P_d}{2} \right)^j \cos\psi \qquad (21.107)$$

The angular extent of the bearing arc $2\psi_l$ in which the rolling elements are loaded is obtained by setting the root expression in Eq. (21.107) equal to zero and solving for ψ:

$$\psi_l = \cos^{-1} \left(\frac{P_d}{2\delta} \right)$$

The summation in Eq. (21.107) applies only to the angular extent of the loaded region. This equation can be written for a roller bearing as

$$F_r = \left(\psi_l - \frac{P_d}{2\delta} \sin \psi_l \right) \frac{nK_1\delta}{2\pi} \qquad (21.108)$$

and similarly in integral form for a ball bearing as

$$F_r = \frac{n}{\pi} K_{1.5}\delta^{3/2} \int_0^{\psi_l} \left(\cos \psi - \frac{P_d}{2\delta} \right)^{3/2} \cos \psi \, d\psi$$

The integral in the equation can be reduced to a standard elliptic integral by the hypergeometric series and the beta function. If the integral is numerically evaluated directly, the following approximate expression is derived:

$$\int_0^{\psi_l} \left(\cos\psi - \frac{P_d}{2\delta}\right)^{3/2} \cos\psi \, d\psi = 2.491 \left\{ \left[1 + \left(\frac{P_d/2\delta - 1}{1.23}\right)^2 \right]^{1/2} - 1 \right\}$$

This approximate expression fits the exact numerical solution to within $\pm 2\%$ for a complete range of $P_d/2\delta$.

The load carried by the most heavily loaded ball is obtained by substituting $\psi = 0°$ in Eq. (21.107) and dropping the summation sign:

$$F_{\max} = K_j \delta^j \left(1 - \frac{P_d}{2\delta}\right)^j$$

Dividing the maximum ball load [Eq. (21.109)] by the total radial load for a roller bearing [Eq. (21.108)] gives

$$F_r = \frac{[\psi_l - (P_d/2\delta)\sin\psi_l]\, n F_{\max}}{2\pi(1 - P_d/2\delta)} \tag{21.109}$$

and similarly for a ball bearing

$$F_r = \frac{n F_{\max}}{Z} \tag{21.110}$$

where

$$Z = \frac{\pi(1 - P_d/2\delta)^{3/2}}{2.491 \left\{ \left[1 + \left(\dfrac{1 - P_d/2\delta}{1.23}\right)^2 \right]^{1/2} - 1 \right\}} \tag{21.111}$$

For *roller bearings* when the diametral clearance P_d is zero, Eq. (21.105) gives

$$F_r = \frac{n F_{\max}}{4} \tag{21.112}$$

For *ball bearings* when the diametral clearance P_d is zero, the value of Z in Eq. (21.110) becomes 4.37. This is the value derived by Stribeck[46] for ball bearings of zero diametral clearance. The approach used by Stribeck was to evaluate the finite summation for various numbers of balls. He then derived the celebrated Stribeck equation for static load-carrying capacity by writing the more conservative value of 5 for the theoretical value of 4.37:

$$F_r = \frac{n F_{\max}}{5} \tag{21.113}$$

In using Eq. (21.113), it should be remembered that Z was considered to be a constant and that the effects of clearance and applied load on load distribution were not taken into account. However, these effects were considered in obtaining Eq. (21.110).

Thrust-Loaded Ball Bearings. The static-thrust-load capacity of a ball bearing may be defined as the maximum thrust load that the bearing can endure before the contact ellipse approaches a race shoulder, as shown in Fig. 21.89, or the load at which the allowable mean compressive stress is reached, whichever is smaller. Both the limiting shoulder height and the mean compressive stress must be calculated to find the static-thrust-load capacity.

The contact ellipse in a bearing race under a load is shown in Fig. 21.89. Each ball is subjected to an identical thrust component F_t/n, where F_t is the total thrust load. The initial contact angle before the application of a thrust load is denoted by β_f. Under load, the normal ball thrust load F acts at the contact angle β and is written as

$$F = \frac{F_t}{n} \sin\beta \tag{21.114}$$
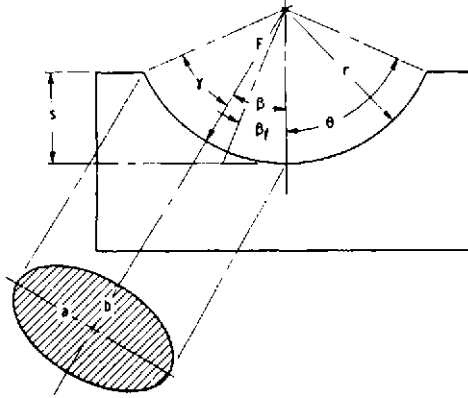
Fig. 21.89   Contact ellipse in bearing race. (From Ref. 10.)

A cross section through an angular-contact bearing under a thrust load F_t is shown in Fig. 21.90. From this figure the contact angle after the thrust load has been applied can be written as

$$\beta = \cos^{-1}\left(\frac{D - P_d/2}{D + \delta}\right) \tag{21.115}$$

The initial contact angle was given in Eq. (21.74). Using that equation and rearranging terms in Eq. (21.115) give, solely from geometry (Fig. 21.90),

Fig. 21.90   Angular-contact ball bearing under thrust load. (From Ref. 10.)

$$\delta = D\left(\frac{\cos \beta_f}{\cos \beta} - 1\right) = \delta_o + \delta_i$$

$$= \left[\frac{F}{(K_j)_o}\right]^{1/j} + \left[\frac{F}{(K_j)_i}\right]^{1/j}$$

$$K_j = 1 \bigg/ \left\{\left[\frac{1}{(K_j)_o}\right]^{1/j} + \left[\frac{1}{(K_j)_i}\right]^{1/j}\right\}^j$$

$$K_j = 1 \bigg/ \left\{\left[\frac{4.5\,\mathfrak{I}_o^3}{\pi k_o E_o'(R_o\,\mathfrak{s}_o)^{1/2}}\right]^{2/3} + \left[\frac{4.5\,\mathfrak{I}_i^3}{\pi k_i E_i(R_i\,\mathfrak{s}_i)^{1/2}}\right]^{2/3}\right\} \tag{21.116}$$

$$F = K_j D^{3/2}\left(\frac{\cos \beta_f}{\cos \beta} - 1\right)^{3/2} \tag{21.117}$$

where

$$K_{1.5} = \pi k E'\left(\frac{R\,\mathfrak{s}}{4.5\,\mathfrak{I}^3}\right)^{1/2} \tag{21.118}$$

and k, $\mathfrak{s}$, and $\mathfrak{I}$ are given by Eqs. (21.39), (21.40), and (21.41), respectively.

From Eqs. (21.114) and (21.117), we can write
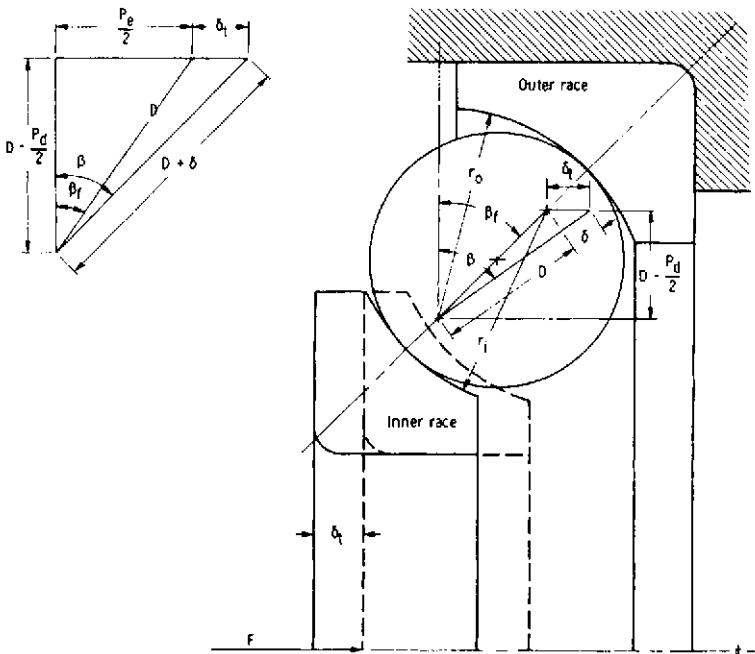
$$\frac{F_t}{n\sin \beta} = F$$

$$\frac{F_t}{nK_j D^{3/2}} = \sin \beta \left(\frac{\cos \beta_f}{\cos \beta} - 1\right)^{3/2} \tag{21.119}$$

This equation can be solved numerically by the Newton–Raphson method. The iterative equation to be satisfied is

$$\beta' - \beta = \frac{\dfrac{F_t}{nK_{1.5}D^{3/2}} - \sin \beta \left(\dfrac{\cos \beta_f}{\cos \beta} - 1\right)^{3/2}}{\cos \beta\left(\dfrac{\cos \beta_f}{\cos \beta} - 1\right)^{3/2} + \dfrac{3}{2}\cos \beta_f \tan^2 \beta \left(\dfrac{\cos \beta_f}{\cos \beta} - 1\right)^{1/2}} \tag{21.120}$$

In this equation convergence is satisfied when $\beta' - \beta$ becomes essentially zero.

When a thrust load is applied, the shoulder height is limited to the distance by which the pressure–contact ellipse can approach the shoulder. As long as the following inequality is satisfied, the pressure–contact ellipse will not exceed the shoulder height limit:

$$\theta > \beta + \sin^{-1}\left(\frac{D_y}{fd}\right)$$

From Fig. 21.79 and Eq. (21.68), the angle used to define the shoulder height θ can be written as

$$\theta = \cos^{-1}\left(\frac{1-s}{fd}\right)$$

From Fig. 21.77 the axial deflection δ_t corresponding to a thrust load can be written as

$$\delta_t = (D + \delta)\sin \beta - D\sin \beta_f \tag{21.121}$$

Substituting Eq. (21.116) into Eq. (21.121) gives

$$\delta_t = \frac{D\sin(\beta - \beta_f)}{\cos \beta}$$

Having determined β from Eq. (21.120) and β_f from Eq. (21.103), we can easily evaluate the relationship for δ_t.

   Preloading.   The use of angular-contact bearings as duplex pairs preloaded against each other is discussed in the first subsection in Section 21.3.6. As shown in Table 21.10 duplex bearing pairs are used in either back-to-back or face-to-face arrangements. Such bearings are usually preloaded against each other by providing what is called "stickout" in the manufacture of the bearing. This is illustrated in Fig. 21.91 for a bearing pair used in a back-to-back arrangement. The magnitude of the stickout and the bearing design determine the level of preload on each bearing when the bearings are clamped together as in Fig. 21.91. The magnitude of preload and the load–deflection characteristics for a given bearing pair can be calculated by using Eqs. (21.74), (21.99), (21.114), and (21.116)–(21.119).

   The relationship of initial preload, system load, and final load for bearings a and b is shown in Fig. 21.92. The load–deflection curve follows the relationship $\delta = KF^{2/3}$. When a system thrust load F_t is imposed on the bearing pairs, the magnitude of load on bearing b increases while that on bearing a decreases until the difference equals the system load. The physical situation demands that the change in each bearing deflection be the same ($\Delta a = \Delta b$ in Fig. 21.92). The increments in bearing load, however, are not the same. This is important because it always requires a system thrust load far greater than twice the preload before one bearing becomes unloaded. Prevention of bearing unloading, which can result in skidding and early failure, is an objective of preloading.

Rolling Bearing Fatigue Life

   Contact Fatigue Theory.   Rolling fatigue is a material failure caused by the application of repeated stresses to a small volume of material. It is a unique failure type. It is essentially a process of seeking out the weakest point at which the first failure will occur. A typical spall is shown in Fig. 21.93. We can surmise that on a microscale there will be a wide dispersion in material strength or resistance to fatigue because of inhomogeneities in the material. Because bearing materials are complex alloys, we would not expect them to be homogeneous nor equally resistant to failure at all points. Therefore, the fatigue process can be expected to be one in which a group of supposedly identical specimens exhibit wide variations in failure time when stressed in the same way. For this reason it is necessary to treat the fatigue process statistically.

   To be able to predict how long a typical bearing will run under a specific load, we must have the following two essential pieces of information:

   1.   An accurate, quantitative estimate of the life dispersion or scatter.
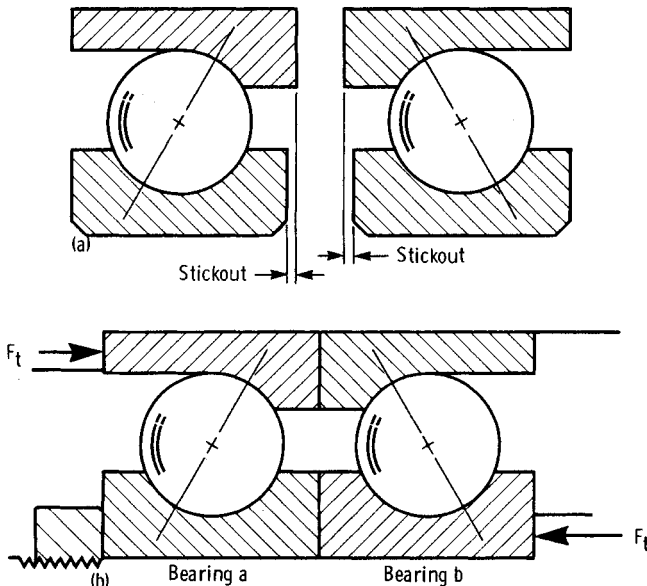
Fig. 21.91   Angular-contact bearings in back-to-back arrangement, shown individually as manufactured and as mounted with preload. (From Ref. 6.) (*a*) Separated. (*b*) Mounted and preloaded.
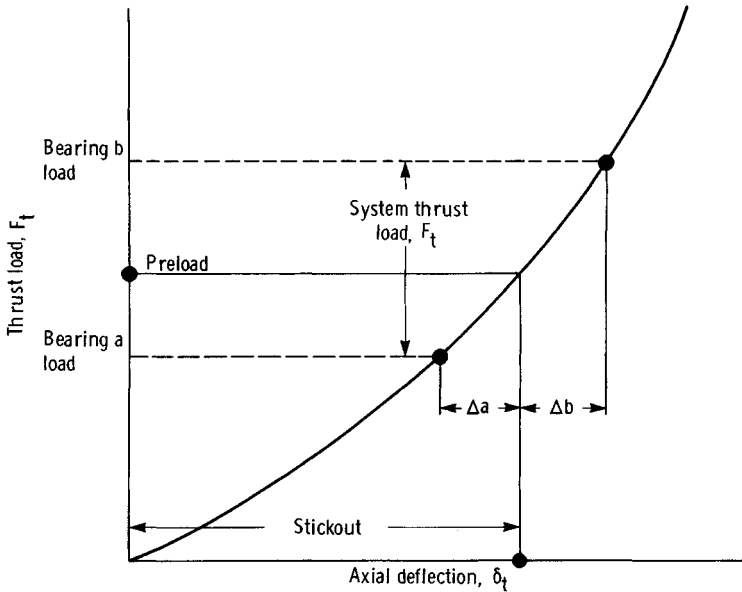
Fig. 21.92 Thrust-load-axial-deflection curve for a typical ball bearing. (From Ref. 6.)

2. The life at a given survival rate or reliability level. This translates into an expression for the "load capacity," or the ability of the bearing to endure a given load for a stipulated number of stress cycles or revolutions. If a group of supposedly identical bearings is tested at a specific load and speed, there will be a wide scatter in bearing lives, as shown in Fig. 21.94.

The Weibull Distribution. Weibull[47] postulates that the fatigue lives of a homogeneous group of rolling-element bearings are dispersed according to the following relation:

$$\ln \frac{1}{S} = e_1 \ln L/A$$
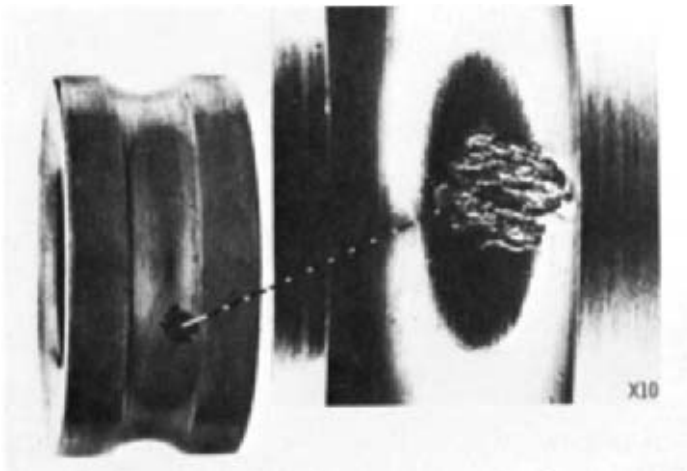
Fig. 21.93 Typical fatigue spall.
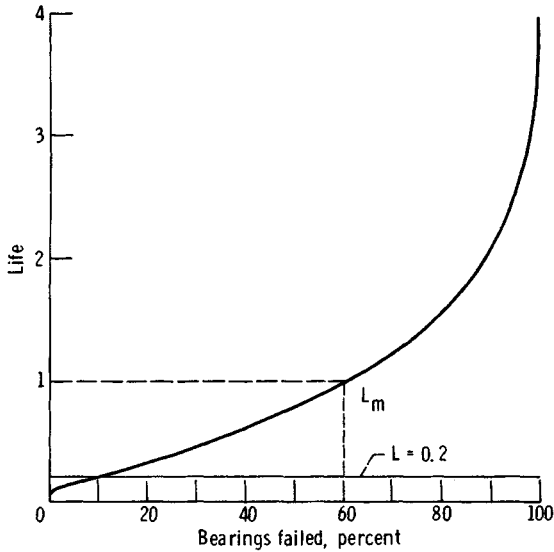
Fig. 21.94 Distribution of bearing fatigue failures. (From Ref. 6.)

where S is the probability of survival, L is the fatigue life, and e_1 and A are constants. The Weibull distribution results from a statistical theory of strength based on probability theory, where the dependence of strength on volume is explained by the dispersion in material strength. This is the "weakest link" theory.

Consider a volume being stressed that is broken up into m similar volumes:

$$S_1 = 1 - M_1 \qquad S_2 = 1 - M_2 \qquad S_3 = 1 - M_3 \qquad \cdots \qquad S_m = 1 - M_m$$
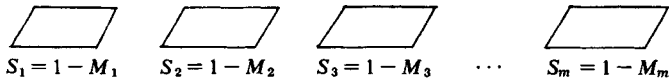
The M's represent the probability of failure and the S's represent the probability of survival. For the entire volume we can write

$$S = S_1 \cdot S_2 \cdot S_3 \cdots \cdots S_m$$

Then

$$1 - M = (1 - M_1)(1 - M_2)(1 - M_3) \cdots (1 - M_m)$$

$$1 - M = \prod_{i=1}^{m} (1 - M_i)$$

$$S = \prod_{i=1}^{m} (1 - M_i)$$

The probability of a crack starting in the ith volume is

$$M_i = f(x)v_i$$

where $f(x)$ is a function of the stress level, the number of stress cycles, and the depth into the material where the maximum stress occurs and v_i is the elementary volume. Therefore,

$$S = \prod_{i=1}^{m} [1 - f(x)v_i]$$

$$\ln S = \sum_{i=1}^{m} \ln[1 - f(x)v_i]$$

Now if $f(x)v_i \ll 1$, then $\ln[1 - f(x)v_i] = -f(x)v_i$ and

$$\ln S = -\sum_{i=1}^{m} f(x)v_i$$

Let $v_i \rightarrow 0$; then

$$\sum_{i=1}^{m} f(x)v_i = \int (x) \, dv = f(x)V$$

Lundberg and Palmgren[48] assume that $f(x)$ could be expressed as a power function of shear stress τ_0, number of stress cycles, J, and depth to the maximum shear stress Z_0:

$$f(x) = \frac{\tau_0^{c_1} J^{c_2}}{Z_0^{c_3}} \tag{21.122}$$

They also choose as the stressed volume

$$V = D_y Z_0 l_v$$

Then

$$\ln S = -\frac{\tau_0^{c_1} J^{c_2} D_y l_v}{Z_0^{c_3-1}}$$

or

$$\ln \frac{1}{S} = \frac{\tau_0^{c_1} J^{c_2} D_y l_v}{Z_0^{c_3-1}}$$

For a specific bearing and load (e.g., stress) τ_0, D_y, l_v, and Z_0 are all constant, so that

$$\ln \frac{1}{S} \approx J^{c_2}$$

Designating J as life L in stress cycles gives

$$\ln \frac{1}{S} = \left(\frac{L}{A}\right)^{c_2}$$

or

$$\ln \ln \frac{1}{S} = c_2 \ln \left(\frac{L}{A}\right) \tag{21.123}$$

This is the Weibull distribution, which relates probability of survival and life. It has two principal functions. First, bearing fatigue lives plot as a straight line on Weibull coordinates (log log vs log), so that the life at any reliability level can be determined. Of most interest are the L_{10} life ($S = 0.9$) and the L_{50} life ($S = 0.5$). Bearing load ratings are based on the L_{10} life. Second, Eq. (21.123) can be used to determine what the L_{10} life must be to obtain a required life at any reliability level. The L_{10} life is calculated, from the load on the bearing and the bearing dynamic capacity or load rating given in manufacturers' catalogs and engineering journals, by using the equation

$$L = \left(\frac{C}{F_e}\right)^m$$

where C = basic dynamic capacity or load rating
      F_e = equivalent bearing load
      m = 3 for elliptical contacts and 10/3 for rectangular contacts

A typical Weibull plot is shown in Fig. 21.95.

Lundberg–Palmgren Theory. The Lundberg–Palmgren theory, on which bearing ratings are based, is expressed by Eq. (21.122). The exponents in this equation are determined experimentally from the dispersion of bearing lives and the dependence of life on load, geometry, and bearing size. As a standard of reference, all bearing load ratings are expressed in terms of the specific dynamic capacity C, which, by definition, is the load that a bearing can carry for 10^6 inner-race revolutions with a 90% chance of survival.

Factors on which specific dynamic capacity and bearing life depend are:

1. Size of rolling element.
2. Number of rolling elements per row.
3. Number of rows of rolling elements.
4. Conformity between rolling elements and races.
5. Contact angle under load.
6. Material properties.
7. Lubricant properties.
8. Operating temperature.
9. Operating speed.

Only factors 1–5 are incorporated in bearing dynamic capacities developed from the Lundberg–Palmgren theory. The remaining factors must be taken into account in the life adjustment factors discussed later.

The formulas for specific dynamic capacity as developed by Lundberg and Palmgren[48,49] are as follows:

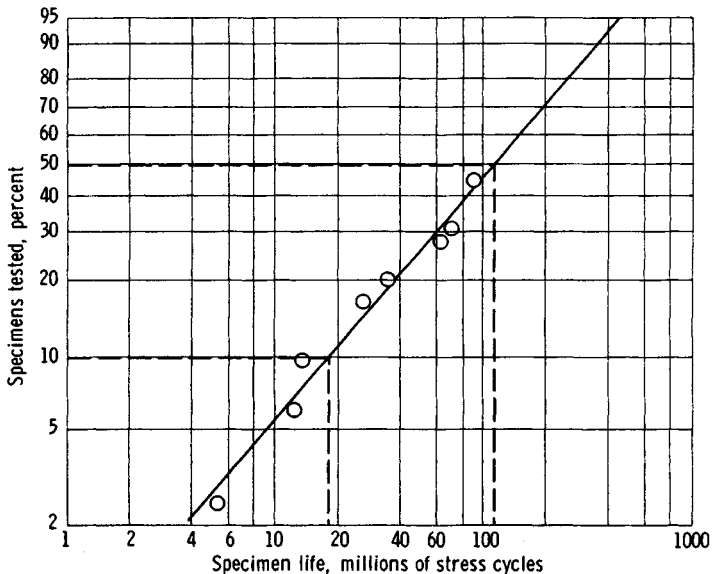For radial ball bearings with $d \leq 25$ mm,

Fig. 21.95 Typical Weibull plot of bearing fatigue failures. (From Ref. 10.)

$$C = f_c(i \cos \beta)^{0.7} n^{2/3} \left(\frac{d}{0.0254}\right)^{1.8}$$

where d = diameter of rolling element, m
  i = number of rows of rolling elements
  n = number of rolling elements per row
  β = contact angle
  f_c = coefficient dependent on material and bearing type

For radial ball bearings with $d \geq 25$ mm,

$$C = f_c(i \cos \beta)^{0.7} n^{2/3} \left(\frac{d}{0.0254}\right)^{1.4}$$

For radial roller bearings,

$$C = f_c(i \cos \beta)^{0.78} n^{3/4} \left(\frac{d}{0.0254}\right)^{1.07} \left(\frac{l_t}{0.0254}\right)^{0.78}$$

where l_t is roller length in meters.
  For thrust ball bearings with $\beta \neq 90°$,

$$C = f_c(i \cos \beta)^{0.7}(\tan \beta)n^{2/3} \left(\frac{d}{0.0254}\right)^{1.8}$$

For thrust roller bearings with $\beta \neq 90°$,

$$C = f_c(i \cos \beta)^{0.78}(\tan \beta)n^{3/4} \left(\frac{l_t}{0.0254}\right)^{0.78}$$

For thrust ball bearings with $\beta = 90°$,

$$C = f_c i^{0.7} n^{2/3} \left(\frac{d}{0.0254}\right)^{1.8}$$

For thrust roller bearings with $\beta = 90°$,

$$C = f_c i^{0.78} n^{3/4} \left(\frac{d}{0.0254}\right)^{1.07} \left(\frac{l_t}{0.0254}\right)^{0.78}$$

For ordinary bearing steels such as SAE 52100 with mineral oil lubrication, f_c can be evaluated by using Tables 21.18 and 21.19, but a more convenient method is to use tabulated values from the most recent Antifriction Bearing Manufacturers Association (AFBMA) documents on dynamic load ratings and life.[50] The value of C is calculated or determined from bearing manufacturers' catalogs. The equivalent load F_e can be calculated from the equation

$$F_e = XF_r + YF_t$$

Factors X and Y are given in bearing manufacturers' catalogs for specific bearings.
  In addition to specific dynamic capacity C, every bearing has a specific static capacity, usually designated as C_0. Specific static capacity is defined as the load that, under static conditions, will result in a permanent deformation of 0.0001 times the rolling-element diameter. For some bearings C_0 is less than C, so it is important to avoid exposing a bearing to a static load that exceeds C_0. Values of C_0 are also given in bearing manufacturers' catalogs.

  The AFBMA Method.   Shortly after publication of the Lundberg–Palmgren theory, the AFBMA began efforts to standardize methods for establishing bearing load ratings and making life predictions. Standardized methods of establishing load ratings for ball bearings[51] and roller bearings[52] were devised, based essentially on the Lundberg–Palmgren theory. These early standards are published in their entirety in Jones.[45] In recent years significant advances have been made in rolling-element bearing material quality and in our understanding of the role of lubrication in bearing life through the development of elastohydrodynamic theory. Therefore the original AFBMA standards in

Table 21.18 Capacity Formulas for Rectangular and Elliptic Contacts[a] (From Ref. 6)

Function	Elliptical Contact of Ball Bearings			Rectangular Contact of Roller Bearings		
c	$f_c f_a i^{0.7} N^{2/3} d^{1.8}$			$f_c f_a i^{7/9} N^{3/4} d^{29/27} l_{t,i}^{7/9}$		
f_c	$g_c f_1 f_2 \left(\dfrac{d_i}{d_i - d}\right)^{0.41}$			$g_c f_1 f_2$		
g_c	$\left[1 + \left(\dfrac{c_i}{c_o}\right)^{10/8}\right]^{-0.8}$			$\left[1 + \left(\dfrac{c_i}{c_o}\right)^{9/2}\right]^{-2/9}$		
c_i/c_o	$f_3 \left[\dfrac{d_i(d_o - d)}{d_o(d_i - d)}\right]^{0.41}$			$f_3 \left(\dfrac{l_{t,i}}{l_{t,o}}\right)^{7/9}$		
	Radial	**Thrust** $\beta \neq 90°$	**Thrust** $\beta = 90°$	**Radial**	**Thrust** $\beta \neq 90°$	**Thrust** $\beta = 90°$
γ	$\dfrac{d \cos \beta}{d_e}$		$\dfrac{d}{d_e}$	$\dfrac{d \cos \beta}{d_e}$		$\dfrac{d}{d_e}$
f_a	$(\cos \beta)^{0.7}$	$(\cos \beta)^{0.7} \tan \beta$	1	$(\cos \beta)^{7/9}$	$(\cos \beta)^{7/9} \tan \beta$	1
f_1	$3.7\text{–}4.1$	$6\text{–}10$		$18\text{–}25$	$36\text{–}60$	
f_2	$\dfrac{\gamma^{0.3}(1 - \gamma)^{1.39}}{(1 + \gamma)^{1/3}}$		$\gamma^{0.3}$	$\dfrac{\gamma^{2/9}(1 - \gamma)^{29/27}}{(1 + \gamma)^{1/3}}$		$\gamma^{2/9}$
f_3	$104 f_4$	f_4	1	$1.14 f_4$	f_4	1
f_4	$\left(\dfrac{1 - \gamma}{1 + \gamma}\right)^{1.72}$			$\left(\dfrac{1 - \gamma}{1 + \gamma}\right)^{38/37}$		

[a]Units in kg and mm.

AFBMA[51,52] have been updated with life adjustment factors. These factors have been incorporated into ISO,[50] which is discussed in the following section.

Life Adjustment Factors. A comprehensive study of the factors affecting the fatigue life of bearings, which were not taken account of in the Lundberg–Palmgren theory, is reported in Bamberger et al.[53] In that reference it was assumed that the various environmental or bearing design factors are multiplicative in their effect on bearing life. The following equation results:

$$L_A = (\tilde{D})(\tilde{E})(\tilde{F})(\tilde{G})(\tilde{H})L_{10}$$

or

$$L_A = (\tilde{D})(\tilde{E})(\tilde{F})(\tilde{G})(\tilde{H})(C/F_e)^m$$

where $\tilde{D}$ = materials factor
   $\tilde{E}$ = metallurgical processing factor
   $\tilde{F}$ = lubrication factor
   $\tilde{G}$ = speed effect factor
   $\tilde{H}$ = misalignment factor
   F_e = bearing equivalent load
   m = load-life exponent; either 3 for ball bearings or 10/3 for roller bearings

Factors, $\tilde{D}$, $\tilde{E}$, and $\tilde{F}$ are briefly reviewed here. The reader is referred to Bamberger et al.[53] for a complete discussion of all five life adjustment factors.

Materials Factors $\tilde{D}$ and $\tilde{E}$. For over a century, AISI 52100 steel has been the predominant material for rolling-element bearings. In fact, the basic dynamic capacity as defined by AFBMA in 1949 is based on an air-melted 52100 steel, hardened to at least Rockwell C 58. Since that time, better control of air-melting processes and the introduction of vacuum remelting processes have resulted in more homogeneous steels with fewer impurities. Such steels have extended rolling-element bearing fatigue lives to several times the AFBMA or catalog life. Life improvements of 3–8 times are not uncommon. Other steel compositions, such as AISI M-1 and AISI M-50, chosen for their

**Table 21.19 Capacity Formulas for Mixed Rectangular and Elliptical Contacts[a]
(From Ref. 6)**

Function	Radial Bearing	Thrust Bearing $\beta \neq 90°$	Thrust Bearing $\beta = 90°$	Radial Bearing	Thrust Bearing $\beta \neq 90°$	Thrust Bearing $\beta = 90°$
	Inner Race			Outer Race		
γ	$\dfrac{d \cos \beta}{d_e}$		$\dfrac{d}{d_e}$	$\dfrac{d \cos \beta}{d_e}$		$\dfrac{d}{d_e}$
	Rectangular Contact c_i			Elliptical Contact c_o		
c_i or c_o	$f_1 f_2 f_a i^{7/9} N^{3/4} D^{29/27} l_{t,i}^{7/9}$			$f_1 f_2 f_a \left(\dfrac{2R}{D}\dfrac{r_o}{r_o - R}\right)^{0.41} i^{0.7} N^{2/3} D^{1.8}$		
f_a	$(\cos \beta)^{7/9}$	$(\cos \beta)^{7/9} \tan \beta$	1	$(\cos \beta)^{0.7}$	$(\cos \beta)^{0.7} \tan \beta$	1
f_1	18–25	36–60		3.5–3.9	6–10	
f_2	$\dfrac{\gamma^{2/9}(1-\gamma)^{29/27}}{(1+\gamma)^{1/3}}$		$\gamma^{3/9}$	$\dfrac{\gamma^{0.3}(1+\gamma)^{1.39}}{(1-\gamma)^{1/3}}$		$\gamma^{0.3}$
	Point Contact c_i			Line Contact c_o		
c_i or c_o	$f_1 f_2 f_a \left(\dfrac{2R}{D}\dfrac{r_i}{r_i - R}\right)^{0.41} i^{0.7} n^{2/3} d^{1.8}$			$f_1 f_2 f_a i^{7/9} n^{3/4} d^{29/27} l_{t,o}^{7.9}$		
f_a	$(\cos \alpha)^{0.7}$	$(\cos \alpha)^{0.7} \tan \alpha$	1	$(\cos \alpha)^{7/9}$	$(\cos \alpha)^{7/9} \tan \alpha$	1
f_1	3.7–4.1	6–10		15–22	36–60	
f_2	$\dfrac{\gamma^{0.3}(1-\gamma)^{1.39}}{(1+\gamma)^{1/3}}$		$\gamma^{0.3}$	$\dfrac{\gamma^{2/9}(1+\gamma)^{29/27}}{(1-\gamma)^{1/3}}$		$\gamma^{2/9}$

[a]$C = C_i [1 + (C_i/C_o)^4]^{1/4}$ units in kg and mm.

higher-temperature capabilities and resistance to corrosion, also have shown greater resistance to fatigue pitting when vacuum melting techniques are employed. Case-hardened materials, such as AISI 4620, AISI 4118, and AISI 8620, used primarily for roller bearings, have the advantage of a tough, ductile steel core with a hard, fatigue-resistant surface.

The recommended $\tilde{D}$ factors for various alloys processed by air melting are shown in Table 21.20. Insufficient definitive life data were found for case-hardened materials to recommended $\tilde{D}$ factors for

Table 21.20 Material Factor for Through-Hardened Bearing Materials[a] (From Ref. 53)

Material	$\tilde{D}$-Factor
52100	2.0
M-1	.6
M-2	.6
M-10	2.0
M-50	2.0
T-1	.6
Halmo	2.0
M-42	.2
WB 49	.6
440C	0.6–0.8

[a]Air-melted materials assumed.

them. It is recommended that the user refer to the bearing manufacturer for the choice of a specific case-hardened material.

The metallurgical processing variables considered in the development of the $\tilde{E}$ factor included melting practice (air and vacuum melting) and metal working (thermomechanical working). Thermomechanical working of M-50 has also been shown to result in improved life, but it is costly and still not fully developed as a processing technique. Bamberger et al.[53] recommended an $\tilde{E}$ factor of 3 for consumable-electrode-vacuum-melted materials.

The translation of factors into a standard[50] is discussed later.

Lubrication Factor $\tilde{F}$. Until approximately 1960 the role of the lubricant between surfaces in rolling contact was not fully appreciated. Metal-to-metal contact was presumed to occur in all applications with attendant required boundary lubrication. The development of elastohydrodynamic lubrication theory showed that lubricant films of thickness of the order of microinches and tens of microinches occur in rolling contact. Since surface finishes are of the same order of magnitude as the lubricant film thicknesses, the significance of rolling-element bearing surface roughnesses to bearing performance became apparent. Tallian[54] first reported on the importance on bearing life of the ratio of elastohydrodynamic lubrication film thickness to surface roughness. Figure 21.96 shows life as a percentage of calculated L_{10} life as a function of Λ, where

$$\Lambda = \frac{h_{min}}{(\Delta_a^2 + \Delta_b^2)^{1/2}}$$

Figure 21.97, from Bamberger et al.,[53] presents a curve of the recommended $\tilde{F}$ factor as a function of the Λ parameter. A mean of the curves presented in Tallian[54] for ball bearings and in Skurka[55] for roller bearings is recommended for use. A formula for calculating the minimum film thickness h_{min} in the hard-EHL regime is given in Eq. (21.57).

The results of Bamberger et al.[53] have not been fully accepted into the current AFBMA standard represented by ISO.[50] The standard presents the following:

1. Life and dynamic load rating formulas for radial and thrust ball bearings and radial and thrust roller bearings.
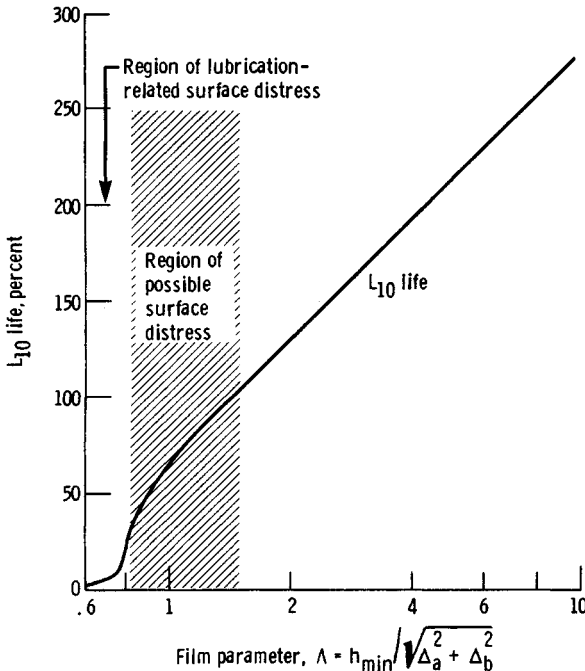

Fig. 21.96 Chart for determining group fatigue life L_{10}. (From Ref. 54.)
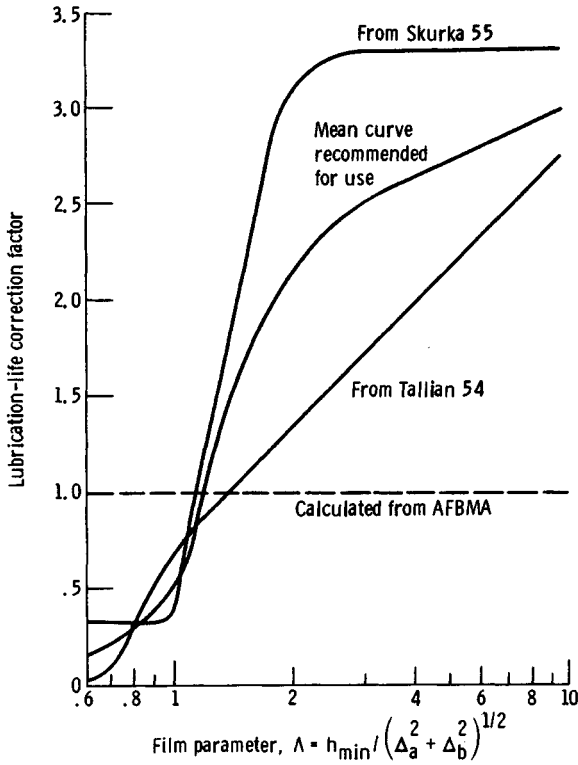
Fig. 21.97 Chart for determining lubrication-life correction factor. (From Ref. 53.)

2. Tables of f_c for all cases.
3. Tables of X and Y factors for calculating equivalent loads.
4. Load rating formulas for multirow bearings.
5. Life correction factors for high-reliability levels a_1, materials a_2, and lubrication or operating conditions a_3.

Procedures for calculating a_2 and a_3 are less than definitive, reflecting the need for additional research, life data, and operating experience.

Applications

In this section two applications of the film thickness equations developed throughout this chapter are presented to illustrate how the fluid-film lubrication conditions in machine elements can be analyzed. Specifically, a typical roller bearing and a typical ball bearing problem are considered.

Cylindrical-Roller-Bearing Problem. The equations for elastohydrodynamic film thickness that have been developed earlier relate primarily to elliptical contacts, but they are sufficiently general to allow them to be used with adequate accuracy in line-contact problems, as would be found in a cylindrical roller bearing. Therefore, the minimum elastohydrodynamic film thicknesses on the inner and outer races of a cylindrical roller bearing with the following dimensions are calculated:

Inner-race diameter, d_i, mm (m)	65 (0.064)
Outer-race diameter, d_o, mm (m)	96 (0.096)
Diameter of cylindrical rollers, d, mm (m)	16 (0.016)
Axial length of cylindrical rollers, l, mm (m)	16 (0.016)
Number of rollers in complete bearing, n	9

A bearing of this kind might well experience the following operating conditions:

Radial load, F_r, N   10,800

Inner-race angular velocity, ω_i, rad/sec   524

Outer-race angular velocity, ω_o, rad/sec   0

Lubricant viscosity at atmospheric pressure at
   operating temperature of bearings, η_o,
   N sec/m^2 0.01

Viscosity–pressure coefficient, ξ, m^2/N 2.2×10^{-8}

Modulus of elasticity for both rollers and races,
   E, N/m^2 2.075×10^{11}

Poisson's ratio, ν 0.3

Calculation. From Eq. (21.124), the most heavily loaded roller can be expressed as

$$F_{max} = \frac{4F_r}{n} = \frac{4(10{,}800 \text{ N})}{9} = 4800 \text{ N} \tag{21.124}$$

Therefore, the radial load per unit length on the most heavily loaded roller is

$$F'_{max} = \frac{4800 \text{ N}}{0.016 \text{ m}} = 0.3 \text{ MN/m} \tag{21.125}$$

From Fig. 21.98 we can write the radii of curvature as

$$r_{ax} = 0.008 \text{ m}, \quad r_{ay} = \infty$$

$$r_{bx,i} = 0.032 \text{ m}, \quad r_{by,i} = \infty$$

$$r_{bx,o} = 0.048 \text{ m}, \quad r_{by,o} = \infty$$

Then

$$\frac{1}{R_{x,i}} = \frac{1}{0.008} + \frac{1}{0.032} = \frac{5}{0.032}$$

giving $R_{x,i} = 0.0064$ m,

$$\frac{1}{R_{x,o}} = \frac{1}{0.008} - \frac{1}{0.048} = \frac{5}{0.048} \tag{21.126}$$
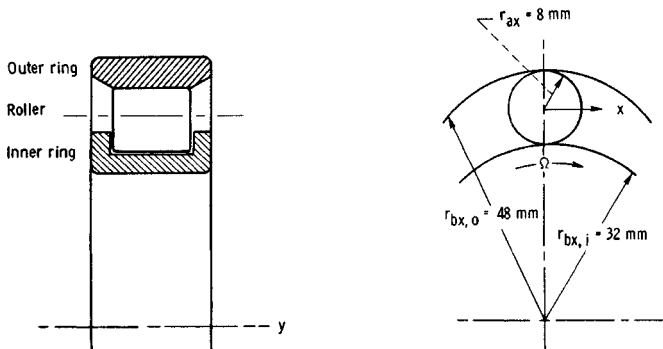
giving $R_{x,o} = 0.0096$ m, and

Fig. 21.98 Roller bearing example: $r_{ay} = r_{by,f} = r_{by,o} = \infty$.

$$\frac{1}{R_{y,i}} = \frac{1}{R_{y,o}} = \frac{1}{\infty} + \frac{1}{\infty} = 0 \tag{21.127}$$

giving $R_{y,i} = R_{y,o} = \infty$.

From the input information, the effective modulus of elasticity can be written as

$$E' = 2 \left(\frac{1 - \nu_a^2}{E_a} + \frac{1 - \nu_b^2}{E_b} \right) = 2.28 \times 10^{11} \text{ N/m}^2 \tag{21.128}$$

For pure rolling, the surface velocity u relative to the lubricated conjunctions for a cylindrical roller is

$$u = |\omega_i - \omega_o| \frac{d_e^2 - d^2}{4d_e} \tag{21.129}$$

where d_e is the pitch diameter and d is the roller diameter.

$$d_e = \frac{d_o + d_i}{2} = \frac{0.096 + 0.064}{2} = 0.08 \text{ m} \tag{21.130}$$

Hence,

$$u = \frac{0.08^2 - 0.16^2}{4 \times 0.08} |524 - 0| = 10.061 \text{ m/sec} \tag{21.131}$$

The dimensionless speed, materials, and load parameters for the inner- and outer-race conjunctions thus become

$$U_i = \frac{\eta_0 u}{E' R_{x,i}} = \frac{0.01 \times 10.061}{2.28 \times 10^{11} \times 0.0064} = 6.895 \times 10^{-11} \tag{21.132}$$

$$G_i = \xi E' = 5016 \tag{21.133}$$

$$W_i = \frac{F}{E'(R_{x,i})^2} = \frac{4800}{2.28 \times 10^{11} \times (0.0064)^2} = 5.140 \times 10^{-4} \tag{21.134}$$

$$U_o = \frac{\eta_0 u}{E' R_{x,o}} = \frac{0.01 \times 10.061}{2.28 \times 10^{11} \times 0.0096} = 4.597 \times 10^{-11} \tag{21.135}$$

$$G_o = \xi E' = 5016 \tag{21.136}$$

$$W_o = \frac{F}{E'(R_{x,o})^2} = \frac{4800}{2.28 \times 10^{11} \times (0.0096)^2} = 2.284 \times 10^{-4} \tag{21.137}$$

The appropriate elliptical-contact elastohydrodynamic film thickness equation for a fully flooded conjunction is developed in Section 21.3.3 and recorded as Eq. (21.138):

$$H_{min} = \frac{h_{min}}{R_x} = 3.63 \, U^{0.68} G^{0.49} W^{-0.073} (1 - e^{-0.68k}) \tag{21.138}$$

For a roller bearing, $k = \infty$ and this equation reduces to

$$H_{min} = 3.63 U^{0.68} G^{0.49} W^{-0.073}$$

The dimensionless film thickness for the roller–inner-race conjunction is

$$H_{min} = \frac{h_{min}}{R_{x,i}} = 3.63 \times 1.231 \times 10^{-7} \times 65.04 \times 1.783 = 50.5 \times 10^{-6}$$

and hence

$$h_{min} = 0.0064 \times 50.5 \times 10^{-6} = 0.32 \ \mu m$$

The dimensionless film thickness for the roller–outer-race conjunction is

$$H_{min} = \frac{h_{min}}{R_{x,o}} = 3.63 \times 9.343 \times 10^{-8} \times 65.04 \times 1.844 = 40.7 \times 10^{-6}$$

and hence

$$h_{min} = 0.0096 \times 40.7 \times 10^{-6} = 0.39 \ \mu m$$

It is clear from these calculations that the smaller minimum film thickness in the bearing occurs at the roller–inner-race conjunction, where the geometrical conformity is less favorable. It was found that if the ratio of minimum film thickness to composite surface roughness is greater than 3, an adequate elastohydrodynamic film is maintained. This implies that a composite surface roughness of $< 0.1 \ \mu m$ is needed to ensure that an elastohydrodynamic film is maintained.

Radial Ball Bearing Problem. Consider a single-row, radial, deep-groove ball bearing with the following dimensions:

Inner-race diameter, d_i, m	0.052291
Outer-race diameter, d_o, m	0.077706
Ball diameter, d, m	0.012700
Number of balls in complete bearing, n	9
Inner-groove radius, r_i, m	0.006604
Outer-groove radius, r_o, m	0.006604
Contact angle, β, deg	0
rms surface finish of balls, Δ_b, μm	0.0625
rms surface finish of races, Δ_a, μm	0.175

A bearing of this kind might well experience the following operating conditions:

Radial load, F_r, N	8900
Inner-race angular velocity, ω_i, rad/sec	400
Outer-race angular velocity, ω_o, rad/sec	0
Lubricant viscosity at atmospheric pressure and effective operating temperature of bearing, η_0, N sec/m^2	0.04
Viscosity–pressure coefficient, ξ, m^2/N	2.3×10^{-8}
Modulus of elasticity for both balls and races, E, N/m^2	2×10^{11}
Poisson's ratio for both balls and races, ν	0.3

The essential features of the geometry of the inner and outer conjunctions (Figs. 21.75 and 21.76) can be ascertained as follows:

Pitch diameter [Eq. (21.68)]:

$$d_e = 0.5(d_o + d_i) = 0.065 \ m$$

Diametral clearance [Eq. (21.69)]:

$$P_d = d_o - d_i - 2d = 1.5 \times 10^{-5} \ m$$

Race conformity [Eq. (21.70)]:

$$f_i = f_o = \frac{r}{d} = 0.52$$

Equivalent radius [Eq. (21.85)]:

$$R_{x,i} = \frac{d(d_e - d)}{2d_e} = 0.00511 \text{ m}$$

Equivalent radius [Eq. (21.87)]:

$$R_{x,o} = \frac{d(d_e + d)}{2d_e} = 0.00759 \text{ m}$$

Equivalent radius [Eq. (21.86)]:

$$R_{y,i} = \frac{f_i d}{2f_i - 1} = 0.165 \text{ m}$$

Equivalent radius [Eq. (21.88)]:

$$R_{y,o} = \frac{f_o d}{2f_o - 1} = 0.165 \text{ m}$$

The curvature sum

$$\frac{1}{R_i} = \frac{1}{R_{x,i}} + \frac{1}{R_{y,i}} = 201.76 \qquad (21.139)$$

gives $R_i = 4.956 \times 10^{-3}$ m, and the curvature sum

$$\frac{1}{R_o} = \frac{1}{R_{x,o}} + \frac{1}{R_{y,o}} = 137.81 \qquad (21.140)$$

gives $R_o = 7.256 \times 10^{-3}$ m. Also, $\alpha_i = R_{y,i}/R_{x,i} = 32.35$ and $\alpha_o = R_{y,o}/R_{x,o} = 21.74$.
The nature of the Hertzian contact conditions can now be assessed.
Ellipticity parameters:

$$k_i = \alpha_i^{2/\pi} = 9.42, \qquad k_o = \alpha_o^{2/\pi} = 7.09 \qquad (21.141)$$

Elliptic integrals:

$$q = \frac{\pi}{2} - 1$$

$$\mathscr{E}_i = 1 + \frac{q}{\alpha_i} = 1.0188, \qquad \mathscr{E}_o = 1 + \frac{q}{\alpha_o} = 1.0278 \qquad (21.142)$$

$$\mathscr{F}_i = \frac{\pi}{2} + q \ln \alpha_i = 3.6205, \qquad \mathscr{F}_o = \frac{\pi}{2} + q \ln \alpha_o = 3.3823 \qquad (21.143)$$

The effective elastic modulus E' is given by

$$E' = 2 \left(\frac{1 - v_a^2}{E_a} + \frac{1 - v_b^2}{E_b} \right)^{-1} = 2.198 \times 10^{11} \text{ N/m}^2$$

To determine the load carried by the most heavily loaded ball in the bearing, it is necessary to adopt an iterative procedure based on the calculation of local static compression and the analysis presented in the fourth subsection in Section 21.3.6. Stribeck[46] found that the value of Z was about 4.37 in the expression

$$F_{\text{max}} = \frac{ZF_r}{n}$$

where F_{max} = load on most heavily loaded ball
F_r = radial load on bearing
n = number of balls

However, it is customary to adopt a value of $Z = 5$ in simple calculations in order to produce a conservative design, and this value will be used to begin the iterative procedure.

Stage 1.   Assume $Z = 5$. Then

$$F_{max} = \frac{5F_r}{9} = \frac{5}{9} \times 8900 = 4944 \text{ N} \tag{21.144}$$

The maximum local elastic compression is

$$\delta_i = \mathfrak{I}_i \left[\left(\frac{9}{2\mathfrak{I}_i R_i} \right) \left(\frac{F_{max}}{\pi k_i E'} \right)^2 \right]^{1/3} = 2.902 \times 10^{-5} \text{ m}$$

$$\delta_o = \mathfrak{I}_o \left[\left(\frac{9}{2\mathfrak{I}_o R_o} \right) \left(\frac{F_{max}}{\pi k_o E'} \right)^2 \right]^{1/3} = 2.877 \times 10^{-5} \text{ m} \tag{21.145}$$

The sum of the local compressions on the inner and outer races is

$$\delta = \delta_i + \delta_o = 5.799 \times 10^{-5} \text{ m}$$

A better value for Z can now be obtained from

$$Z = \frac{\pi (1 - P_d/2\delta)^{3/2}}{2.491 \left\{ \left[1 + \left(\frac{1 - P_d/2\delta}{1.23} \right)^2 \right]^{1/2} - 1 \right\}}$$

since $P_d/2\delta = (1.5 \times 10^{-5})/(5.779 \times 10^{-5}) = 0.1298$. Thus

$$Z = 4.551$$

Stage 2.

$$Z = 4.551$$
$$F_{max} = (4.551 \times 8900)/9 = 4500 \text{ N}$$
$$\delta_i = 2.725 \times 10^{-5} \text{ m}, \qquad \delta_o = 2.702 \times 10^{-5} \text{ m}$$
$$\delta = 5.427 \times 10^{-5} \text{ m}$$
$$\frac{P_d}{2\delta} = 0.1382$$

Thus

$$Z = 4.565$$

Stage 3.

$$Z = 4.565$$
$$F_{max} = \frac{4.565 \times 8900}{9} = 4514 \text{ N}$$
$$\delta_i = 2.731 \times 10^{-5} \text{ m}, \qquad \delta_o = 2.708 \times 10^{-5} \text{ m}$$
$$\delta = 5.439 \times 10^{-5} \text{ m}$$
$$\frac{P_d}{2\delta} = 0.1379$$

and hence

$$Z = 4.564$$

This value is very close to the previous value from stage 2 of 4.565, and a further iteration confirms its accuracy.

Stage 4.

$$Z = 4.564$$

$$F_{max} = \frac{4.564 \times 8900}{9} = 4513 \text{ N}$$

$$\delta_i = 2.731 \times 10^{-5} \text{ m}, \qquad \delta_o = 2.707 \times 10^{-5} \text{ m}$$

$$\delta = 5.438 \times 10^{-5} \text{ m}$$

$$\frac{P_d}{2\delta} = 0.1379$$

and hence

$$Z = 4.564$$

The load on the most heavily loaded ball is thus 4513 N.

Elastohydrodynamic Minimum Film Thickness. For pure rolling

$$u = |\omega_o - \omega_i| \frac{d_e^2 - d^2}{4d_e} = 6.252 \text{ m/sec} \tag{21.146}$$

The dimensionless speed, materials, and load parameters for the inner- and outer-race conjunctions thus become

$$U_i = \frac{\eta_0 u}{E' R_{x,i}} = \frac{0.04 \times 6.252}{2.198 \times 10^{11} \times 5.11 \times 10^{-3}} = 2.227 \times 10^{-10} \tag{21.147}$$

$$G_i = \xi E' = 2.3 \times 10^{-8} \times 2.198 \times 10^{11} = 5055 \tag{21.148}$$

$$W_i = \frac{F}{E'(R_{x,i})^2} = \frac{4513}{2.198 \times 10^{11} \times (5.11)^2 \times 10^{-6}} = 7.863 \times 10^{-4} \tag{21.149}$$

$$U_o = \frac{\eta_0 u}{E' R_{x,o}} = \frac{0.04 \times 6.252}{2.198 \times 10^{11} \times 7.59 \times 10^{-3}} = 1.499 \times 10^{-10} \tag{21.150}$$

$$G_o = \xi E' = 2.3 \times 10^{-8} \times 2.198 \times 10^{11} = 5055 \tag{21.151}$$

$$W_o = \frac{F}{E'(R_{x,o})^2} = \frac{4513}{2.198 \times 10^{11} \times (7.59)^2 \times 10^{-6}} = 3.564 \times 10^{-4} \tag{21.152}$$

The dimensionless minimum elastohydrodynamic film thickness in a fully flooded elliptical contact is given by

$$H_{min} = \frac{h_{min}}{R_x} = 3.63 U^{0.68} G^{0.49} W^{-0.073} (1 - e^{-0.68k}) \tag{21.153}$$

For the ball-inner-race conjunction it is

$$(H_{min})_i = 3.63 \times 2.732 \times 10^{-7} \times 65.29 \times 1.685 \times 0.9983 \tag{21.154}$$
$$= 1.09 \times 10^{-4}$$

Thus

$$(h_{min})_i = 1.09 \times 10^{-4} R_{x,i} = 0.557 \ \mu\text{m}$$

The lubrication factor Λ discussed in the fifth subsection of Section 21.3.6 was found to play a significant role in determining the fatigue life of rolling-element bearings. In this case

$$\Lambda_i = \frac{(h_{min})_i}{(\Delta_a^2 + \Delta_b^2)^{1/2}} = \frac{0.557 \times 10^{-6}}{[(0.175)^2 + (0.06225)^2]^{1/2} \times 10^{-6}} = 3.00 \tag{21.155}$$

Ball–outer-race conjunction is given by

$$(H_{min})_o = \frac{(h_{min})_o}{R_{x,o}} = 3.63 U_o^{0.68} G^{0.49} W^{-0.073} (1 - e^{-0.68k_o})$$

$$= 3.63 \times 2.087 \times 10^{-7} \times 65.29 \times 1.785 \times 0.9919 \qquad (21.156)$$

$$= 0.876 \times 10^{-4}$$

Thus

$$(h_{min})_o = 0.876 \times 10^{-4} R_{x,o} = 0.665 \ \mu m$$

In this case, the lubrication factor Λ is given by

$$\Lambda_o = \frac{0.665 \times 10^{-6}}{[(0.175)^2 + (0.0625)^2]^{1/2} \times 10^{-6}} = 3.58 \qquad (21.157)$$

Once again, it is evident that the smaller minimum film thickness occurs between the most heavily loaded ball and the inner race. However, in this case the minimum elastohydrodynamic film thickness is about three times the composite surface roughness, and the bearing lubrication can be deemed to be entirely satisfactory. Indeed, it is clear from Fig. 21.97 that very little improvement in the lubrication factor $\tilde{F}$ and thus in the fatigue life of the bearing could be achieved by further improving the minimum film thickness and hence Λ.

21.4 BOUNDARY LUBRICATION

If the pressures in fluid-film-lubricated machine elements are too high, the running speeds are too low, or the surface roughness is too great, penetration of the lubricant film will occur. Contact will take place between asperities, leading to a rise in friction and wear rate. Figure 21.99 (obtained from Bowden and Tabor[56]) shows the behavior of the coefficient of friction in the different lubrication regimes. It is to be noted in this figure that in boundary lubrication, although the friction is much higher than in the hydrodynamic regime, it is still much lower than for unlubricated surfaces. As the running conditions are made more severe, the amount of lubricant breakdown increases, until the system scores or seizes so badly that the machine element can no longer operate successfully.

Figure 21.100 shows the wear rate in the different lubrication regimes as determined by the operating load. In the hydrodynamic and elastohydrodynamic lubrication regimes, since there is no asperity contact, there is little or no wear. In the boundary lubrication regime the degree of asperity interaction and wear rate increases as the load increases. The transition from boundary lubrication to an unlubricated condition is marked by a drastic change in wear rate. Machine elements cannot operate successfully in the unlubricated region. Together Figs. 21.99 and 21.100 show that both friction and wear can be greatly decreased by providing a boundary lubricant to unlubricated surfaces.

Understanding boundary lubrication depends first on recognizing that bearing surfaces have asperities that are large compared with molecular dimensions. On the smoothest machined surfaces these asperities may be 25 nm (0.025 μm) high; on rougher surfaces they may be ten to several hundred times higher. Figure 21.101 illustrates typical surface roughness as a random distribution of
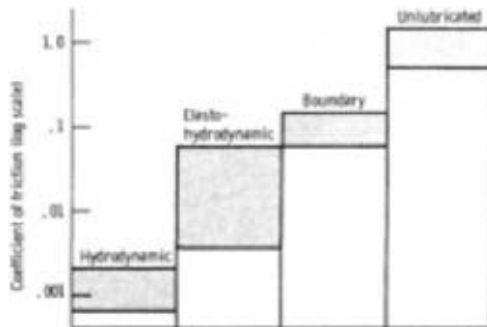
Fig. 21.99 Schematic drawing showing how type of lubrication shifts from hydrodynamic to elastohydrodynamic to boundary lubrication as the severity of running conditions is increased. (From Ref. 56.)